Biophysical Journal
Article

Biophysical Society

# A General Workflow for Characterization of Nernstian Dyes and Their Effects on Bacterial Physiology

Leonardo Mancini,[1] Guillaume Terradot,[1] Tian Tian,[2] YingYing Pu,[2] Yingxing Li,[2] Chien-Jung Lo,[3] Fan Bai,[2] and Teuta Pilizota[1,*]

[1]Centre for Synthetic and Systems Biology, University of Edinburgh, Edinburgh, United Kingdom; [2]Biomedical Pioneering Innovation Center, School of Life Sciences, Peking University, Beijing, China; and [3]Department of Physics and Graduate Institute of Biophysics, National Central University, Jhongli, Taiwan, Republic of China

ABSTRACT The electrical membrane potential ($V_m$) is one of the components of the electrochemical potential of protons across the biological membrane (proton motive force), which powers many vital cellular processes. Because $V_m$ also plays a role in signal transduction, measuring it is of great interest. Over the years, a variety of techniques have been developed for the purpose. In bacteria, given their small size, Nernstian membrane voltage probes are arguably the favorite strategy, and their cytoplasmic accumulation depends on $V_m$ according to the Nernst equation. However, a careful calibration of Nernstian probes that takes into account the tradeoffs between the ease with which the signal from the dye is observed and the dyes' interactions with cellular physiology is rarely performed. Here, we use a mathematical model to understand such tradeoffs and apply the results to assess the applicability of the Thioflavin T dye as a $V_m$ sensor in *Escherichia coli*. We identify the conditions in which the dye turns from a $V_m$ probe into an actuator and, based on the model and experimental results, propose a general workflow for the characterization of Nernstian dye candidates.

SIGNIFICANCE The phospholipid bilayer of a biological membrane is virtually impermeable to charged molecules. Much like in a rechargeable battery, cells harness this property to store an electrical potential that fuels life reactions but also transduces signals. For the case of bacteria, which are small in size and possess a stiff cell wall, arguably the most popular approach to measuring membrane voltage are Nernstian probes, which accumulate across the bacterial membrane according to the Nernst equation. This study characterizes the undesired effects Nernstian probes can have on cell physiology, which can be crucial for the accurate interpretation of experimental results. Using mathematical modeling and experiments, the study provides a general, simple workflow to characterize and minimize these effects.

## INTRODUCTION

Living cells maintain an electric potential difference ($V_m$) across the plasma membrane that acts like a capacitor. This is achieved by active transport of ions:

$$V_m = F \times \frac{Q_{in}}{C}, \quad (1)$$

where $Q_{in}$ is the intracellular charge (in moles), $C$ the membrane capacitance, and $F$ the Faraday constant. Membrane potential stands at the basis of fundamental biological processes such as signal transduction and energy production (1,2). For the latter, $V_m$ adds up to the chemical potential of protons arising from their concentration difference across the membrane to result in the proton electrochemical gradient, the so-called proton motive force (PMF). The PMF drives numerous cellular processes, most notably the production of ATP (2), import of nutrients or osmolites (3–6), and rotation of the bacterial flagellar motor (BFM) (7), and it is necessary for cell division (8).

*Submitted April 12, 2019, and accepted for publication October 18, 2019.*

*Correspondence: teuta.pilizota@ed.ac.uk

Guillaume Terradot and Tian Tian contributed equally to this work.

Editor: Amy Palmer.

https://doi.org/10.1016/j.bpj.2019.10.030

The notion that $V_m$ lies at the very basis of life motivated decades long efforts to measure it (9). The first direct technique dates to 1939 and relies on the mechanical insertion of microelectrodes into squid giant axons (10). The method led to the development of the patch-clamp technique, which advanced the understanding of neuron signal transduction (11–13). However, the applicability of microelectrodes for the measurement of bacterial $V_m$ is limited, owing to the small size of the organisms and the presence of the cell wall (14,15). Some of the subsequently developed methods overcome such limits with the use of molecular sensors (16), grouped into two categories: conformational-change-based sensors and Nernstian sensors. The former are static molecules or proteins that sit inside the membrane or in its close proximity and change conformation or electron distribution in response to changes in $V_m$, which, in turn, affect the optical properties of the chromophores (17–19). Here, we focus on the latter, the Nernstian sensors, and on the parameter range in which they serve as $V_m$ indicators, using *E. coli* as the model organism.

Nernstian sensors are charged molecules that can diffuse across the biological membranes and distribute according to the Nernst equation:

$$V_m = \frac{RT}{zF}\ln\left(\frac{c_{out}}{c_{in}}\right), \tag{2}$$

where $R$, $T$, $z$, $F$, $c_{out}$, and $c_{in}$ denote, respectively, gas constant, temperature, valence of the charged molecule, Faraday's constant, and external and internal concentrations of the charged molecule. For a measurement to be attained, these molecules need to emit a signal that is a proxy for their number. Therefore, Nernstian $V_m$ dyes are usually radiolabeled or fluorescent molecules (16,20), and $V_m$ is calculated from Eq. 2 by measuring the cytoplasmic ($c_{in}$) and the external dye concentrations ($c_{out}$) (21).

However, Nernstian dyes are used in complex biological systems, and a number of factors can be responsible for an incomplete adherence to a fully Nernstian behavior. In Fig. 1, we give a cartoon representation of the tradeoffs imposed on a Nernstian dye by plotting the dye intensity inside *E. coli*'s cytoplasm against the time. The chosen dye concentration should be such that the signal is sufficiently above the background ($\Delta I$ is sufficiently large). Yet, with increasing dye concentration, a cell's $V_m$ is more likely to be affected by the dye. This caveat is inherent to positively charged dyes because these directly lower $V_m$ and more so at higher concentrations (22). The first requirement for a Nernstian dye is thus the existence of a range of concentrations that give sufficient signal without extensively affecting the $V_m$. Likewise, cellular processes should not interfere with the Nernstian behavior of the dye, for example, by actively importing or exporting it. Instead, the dye should be able to diffuse across the membrane, and its diffusion constant will determine the time it takes for the dye to equilibrate across the membrane in agreement with Eq. 2 ($\tau_{eq}$ in Fig. 1). All phenomena that occur quicker than $\tau_{eq}$ are beyond the dye's temporal resolution, and all the measurements taken before $\tau_{eq}$ do not faithfully report $V_m$. Lastly, different dyes bind to the membrane or form aggregates to a different extent (21,23)). However, as long as the dyes do not self-quench at any point (24) or undergo signal enhancements, a constant and well-defined correlation function between the free dye concentration and the signal can be obtained, thus enabling quantitative $V_m$ measurements (most commonly, this is done by separating the signal from the free and bound dye with careful calibration (21,23)).

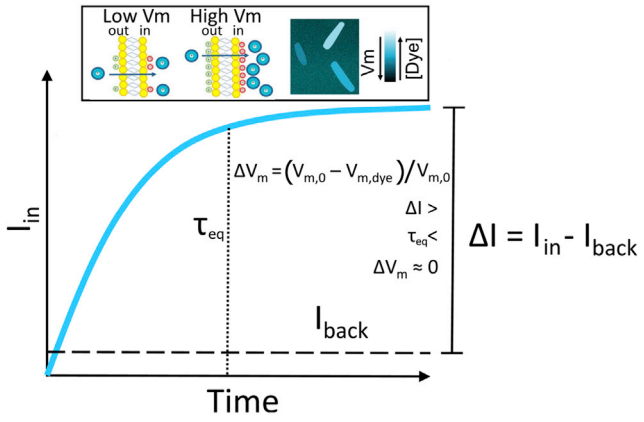


FIGURE 1 A schematic plot of a Nernstian dye equilibration curve. Equilibration time, $\tau_{eq}$, is defined as the time at which the dye internalized by the cell, dye $I_{in}$, reaches 90% of its final value. $V_{m,0}$ and $V_{m,dye}$ indicate the membrane potential before and after the addition of the dye, respectively. $I_{back}$ is the fluorescence intensity of the background. Inset: cartoon showing the mechanism of accumulation of cationic dyes, which accumulate more in cells with a more negative $V_m$. To see this figure in color, go online.

To summarize, to be used as an ideal Nernstian sensor, a cationic dye should 1) give a sufficiently high signal without affecting cell's $V_m$; 2) diffuse through the membrane with $\tau_{eq}$ on the order of minutes; 3) stay inert, despite being charged, and not form bonds or in any way interact with the cell; and 4) have constant signal per molecule. Yet, when using such dyes, these requirements are rarely assessed in a systematic manner before measurements commence. In this work, we identify a workflow that should be adopted, for a given choice of the dye, organism, and external environment, to identify the parameter range in which Nernstian dyes act as sensors rather than actuators, i.e., molecules that actively decrease or increase the $V_m$. We start with a mathematical model that helps us understand relationships and define tradeoffs between dye working concentration and signal intensity, equilibration time, and $V_m$ perturbation. We then show how the identified workflow can be used to benchmark new Nernstian dyes by characterizing the recently reported dye Thioflavin T (ThT) used in *Bacillus subtilis* (25) for use in *E. coli*. We describe the

physiological range in which ThT enables $V_m$ sensing in *E. coli*, and, in the range in which we find it turns into an actuator, we investigate the mechanistic reasons. Our workflow can be applied to the characterization of other Nernstian dyes and provide novel insights for the established ones.

## METHODS

### Bacterial strains

All experiments in which no mutation is explicitly indicated were carried out in the MG1655 strain. For the BFM speed assay, we used MG1655 carrying the FliC-sticky mutation from (26). *ΔtolC* mutants were obtained from the Keio collection (27). Kanamycin resistance of the Keio deletion strain was removed via one-step inactivation with the plasmid pCP20 (28). Kanamycin resistance inactivation and elimination of the pCP20 plasmid were confirmed via kanamycin (50 $\mu$g/mL), chloramphenicol (31 $\mu$g/mL), and ampicillin (100 $\mu$g/mL) sensitivity tests. Both the strain carrying the *ΔtolC* mutation and MG1655 wild type (WT) were transformed with plasmid pTP20-mKate2 (Fig. S1) for cytoplasmic volume measurements. pTP20-mKate2 contains the red fluorescent protein mKate2 and the ribosomal binding site of mCherry. The plasmid was constructed as follows: the backbone from pWR20 (29) and the sequence containing the ribosomal binding site of mCherry and mKate2 were PCR-amplified. The products were purified, cleaved with the restriction enzymes AvrII and NotI (New England Biolabs, Hitchin, UK), and ligated using T4 DNA ligase (Promega, Chilworth, UK). Chemically competent cells were transformed with the ligation mixes, and transformants were confirmed by colony PCR and subsequently sequenced. A map of the plasmid and the primers are given in Fig. S1 and Table S1. All the strains used in the study are summarized in Table S2.

### Bacterial growth conditions

Cells for fluorescence microscopy were grown from an overnight culture by diluting it 1:80 times in Luria-Bertani broth (0.5% yeast extract, 1% Bacto Tryptone, 1% NaCl). The culture was shaken at 220 rpm at 37°C and harvested at $OD_{600}$ = 0.3–0.5. Cells were then washed into fresh LB or MM9 + glucose medium (50 mM $Na_2HPO_4$, 25 mM $NaH_2PO_4$, 8.5 mM NaCl, 18.7 mM NH4Cl, 0.1 mM $CaCl_2$, 1 mM KCl, 2 mM $MgSO_4$, 1× modified Eagle's medium essential amino acids (Gibco, Paisley, UK), and 0.3% glucose). For the simultaneous BFM speed and ThT fluorescence measurements, cells were grown from an overnight culture by diluting it 1:80 times in TB (1% Bacto Tryptone, 0.5% NaCl) at 200 rpm and 30°C. Cells were harvested at $OD_{600}$ = 0.8 as before (30) and washed into fresh MM9 via centrifugation. Growth curves in the presence of ThT were obtained in a Spectrostar Omega microplate reader (BMG, Ortenberg, Germany) using a flat-bottom 96-well plate that was covered with a lid during the experiments (Costar, Glasgow, UK). Each well contained 200 $\mu$L of growth media, either MM9 + glucose or MM9 + glycerol (50 mM $Na_2HPO_4$, 25 mM $NaH_2PO_4$, 8.5 mM NaCl, 18.7 mM NH4Cl, 0.1 mM $CaCl_2$, 1 mM KCl, 2 mM $MgSO_4$, 1× modified Eagle's medium essential amino acids (Gibco), and 0.3% glycerol), and was inoculated with 2 $\mu$L (1:100 dilution) of an overnight culture and a given concentration of ThT. Plates were grown at 37°C with 300 rpm shaking (double orbital mode). ThT (Acros Organics, Loughborough, UK) solutions were prepared from a 10 mM stock of ThT in water made at least monthly and stored at 4°C in the dark.

### Fluorescence microscopy

Imaging was carried out in a custom-built microscope with a 100× oil immersion objective lens (Nikon, Tokyo, Japan) and a neutral white LED as a source of illumination (Cairn Research, Faversham, UK), and images were taken with an iXon Ultra 897 EMCCD camera (Andor, Belfast, UK) (31,32). ThT fluorescence was measured with ZET436/20× and ET525/40 m, and mKate2 and propidium iodide (PI) fluorescence with ET577/25× and ET632/60 m (Chroma Technology, Bellows Falls, VT) excitation and emission filters, respectively. Images were taken at 1 min intervals, exposure time was 50 ms and Andor camera gain 25. We note that ThT undergoes a spectral shift and intensity increase when highly concentrated or when spatially constricted, either by binding to amyloid fibrils or by viscosity (33–35). Our choice of filters aims at minimizing these effects and the damage that shorter wavelengths cause to *E. coli* (36). Cells were imaged in a custom-built flow cell (Fig. S2; (26)) and attached to the coverslip surface as before (26,30). Briefly, 1% poly-L-lysine (Sigma-Aldrich, Gillingham, UK) is flushed through the flow cell and washed with 3–5 mL of growth media after 10 s. Polystyrene particles (beads) with a diameter of 1 $\mu$m (Bangs Laboratories, Fishers, IN), were delivered into the flow cell and allowed to attach to the coverslip surface. After 10 min, unattached beads were flushed away with 1–2 mL of growth media. Next, 200 $\mu$L of cells were delivered to the flow cell and allowed to attach for 10–30 min, after which the unattached cells were removed with 1 mL of growth medium. 10 $\mu$M ThT in growth media was delivered with a peristaltic pump (Fusion 400; Chemyx, Stafford, TX) using 50 $\mu$L/min flow rate while imaging. We deliver 5 $\mu$M of PI stain (MP Biomedicals, Loughborough, UK) in the same way. 5 mM PI stock solution (in water) was stored at 4°C in the dark. Images were stabilized in $x$, $y$, and $z$ positions using a bead attached to the coverslip and back-focal-plane interferometry (29,37). Cells grow attached to the poly-L-lysine surface with expected growth rates (given the medium), as previously reported (38) and seen in Videos S1 and S2.

### Motor speed measurements

Single motor speeds were measured as before (26,30). Briefly, we sheared flagellar filaments by passing them through two syringes with narrow-gauge needles (26 gauge) connected by plastic tubing. The cell attachment protocol was as above, except 0.5 $\mu$m beads (Polysciences, Warrington, PA) were delivered after cell attachment allowing them to attach to filament stubs. Motor speed was measured during continuous flow that delivered MM9 + glucose medium supplemented with 10 $\mu$M ThT. Back-focal-plane interferometry setup and recording conditions are as before (30).

### Data analysis

#### *Motor speed traces*

Raw traces of the position of the bead attached to the filament stub were analyzed by a moving-window discrete Fourier transform as in (30). From the obtained motor speed traces, DC frequency (50 Hz) was removed, speeds lower than 5 Hz were ignored, and subsequently a median filter (window size 11) was applied (26). We note that we use a WT strain for which the BFM can change rotational direction, which appears as a negative speed after application of the moving-window Fourier transform. However, for the purpose of the PMF measurements, these short intervals can be disregarded, and we only show the speed values above 0 Hz.

#### *Fluorescence images*

The image analysis was carried out with custom-written software. From fluorescence images, rectangles containing "flat" cells, i.e., cells that are uniformly attached to the coverslip surface, as well as background rectangles within each cell-containing rectangle, were manually selected (29,37). The edge of the cell was identified within the cell-containing rectangle by applying a global threshold via the Otsu's method (39). Total cells' intensity values were obtained by summing up and averaging pixel belonging to the cells. Values obtained from the background rectangles at the time points

when ThT was loaded in the channel but cells had not taken it up yet were subtracted from the cell intensity values. The beads used for image stabilization stain easily with ThT and were used as a point of reference for dye entry (which, in our case, occurred 7–10 min from the start of imaging). We show fluorescence intensity traces that start at the point of ThT entry but note that cells were exposed to fluorescence illumination in the 7–10 min interval before. For the low fluorescence values characteristic of the early stages of dye equilibration, our script fails to identify cells, in which case we linearly interpolate values between two closest events of successful cell identification. Cell area was measured from intensity profiles, by normalizing them and counting the pixels above 30% of maximum intensity as described previously (29,37).

### *Plate reader data*

Individual growth curves were analyzed with the software deODorizer from (40). To extract the maximum growth rate, three or more repeats in the same condition were aligned by the chosen OD value (usually OD $\sim$ 0.4) using the growth curve that reached it first (in the given condition). The maximum growth rates given in Fig. 3 *C* were normalized by the maximum growth rate in $[\text{Dye}]_{out} = 0$ condition.

## RESULTS

### Mathematical model of Nernstian dye's behavior defines its working parameter range

To predict and understand the mutual effects of dye concentration and cell physiology, we turn to a mathematical model. We assume that the cytoplasmic and extracellular liquids are electrical conductors separated by a membrane, which we treat as a parallel-plate capacitor (Eq. 1; (41,42)). We model the membrane as a single lipid barrier and do not distinguish between the inner and outer membrane of *E. coli*. In the Supporting Materials and Methods, we discuss a more detailed model that includes both membranes and allows for the existence of a small $V_p$ across the outer membrane in addition to the $V_m$ across the inner membrane. We account for four types of charge carriers and assume that all are monovalent to simplify the model without altering the results with respect to $V_m$ dye behavior: 1) negatively charged molecules to which the membrane is close to nonpermeable, denoted $Y$ (this includes surface charges on the inside of the membrane); 2) cationic species actively pumped outward, denoted $C^+$; 3) anionic species, which equilibrate across the membrane $A^-$; and 4) cationic species that equilibrate across the membrane (playing the part of a cationic dye). Thus, $Q_{in}$ is

$$Q_{in} = V_{cell} \times \underbrace{\sum_x z_x [x]_i}_{\text{General Form}}$$

$$= V_{Cell} \times \underbrace{\left([Dye]_{in} + [C^+]_{in} - [A^-]_{in} - [Y]_{in}\right)}_{\text{This manuscript}}, \quad (3)$$

where $V_{cell}$ is the intracellular volume, $z_x$ the valency of species $x$, and $[x]_i$ its intracellular concentration (we only consider $z_x = \pm 1$). The extracellular concentrations and $[Y]_{in}$ are constants set by the initial conditions (we assume that the cell does not affect the ionic composition of its environment, and we treat $[Y]_{in}$ as unable to cross the membrane). We also assume that the cell uses only one type of pumps for cations, and note that $[Dye]_{in}$ and $[Dye]_{out}$ are experimentally determined from fluorescence intensity signal (see Fig. 6 later in the text).

The charge separation, and thus $V_m$, is achieved in the close proximity of the bilayer so that the rest of the cell's cytoplasm stays electroneutral (42,43) and in two ways: first, by pumping $C^+_{in}$ outwards and thus creating a negatively charged intracellular environment, and second, by maintaining $[Y]_{in}$. Pumping $C^+$ outwards against its electrochemical gradient requires free energy, which we consider a constant and label $\Delta G_E$ (where $\Delta G_E < 0$). For example, in the case of a proton/ion antiporter with 1:1 exchange stoichiometry, the free energy is the PMF itself; for a similar antiporter with 2:1 proton/ion stoichiometry, it is 2$\times$ PMF; and for ATP hydrolysis, $\Delta G_E$ is the amount of work given by hydrolyzing one ATP.

The rate at which $C^+$ is pumped out of the whole cell, given in mol/m$^3$/s, is

$$j_P = k_P \times \left(1 - e^{\Delta G_P/(RT)}\right), \quad (4)$$

where $k_P$ is a function that describes the specifics of the transport mechanism by a given pump; here, we keep it a constant. $\Delta G_P$ depends on the electrochemical potential of the pumped cation ($\Delta G_{C^+}$) and $\Delta G_E$. Therefore, the rate of pumping (positive flux means $C^+$ is extruded) depends on the intracellular ionic composition via $V_m$ and $[C^+]_{in}$:

$$\Delta G_P = \Delta G_E - \Delta G_{C^+}, \quad (5)$$

$$\Delta G_{C^+} = F \times V_m + RT \times \ln\left(\frac{[C^+]_{in}}{[C^+]_{out}}\right). \quad (6)$$

Note that for the pump to move $C^+$ outward, $j_P > 0$, and consequently $\Delta G_E < \Delta G_{C^+}$, i.e., the free-energy-providing reaction has to be able to overcome the electrochemical gradient of the $C^+$. The chosen functional dependency of $j_P$ gives the simplest pump kinetics, sufficient for our purpose, that can be expanded to include more complex pumping scenarios (44).

Finally, the dye, the anion, and the cation leak through the membrane (positive flux means $x$ is moved inward) at the rate

$$j_{L,x} = k_{L,x} \times \left(1 - e^{\Delta G_x/(RT)}\right), x \in \{Dye, C^+, A^-\}, \quad (7)$$

$$\Delta G_x = F \times V_m + RT \times \ln\left(\frac{[x]_{in}}{[x]_{out}}\right). \quad (8)$$

Similarly to $k_P$, $k_{L,x}$ is a function whose shape depends on the mechanisms by which an ion leaks across the *E. coli* membrane, which, in turn, depends on the electrostatic potential at a position $z$ within the membrane, $V(z)$. To the best of our knowledge, $V(z)$, and consequently $dV(z)/dz$, is not known for *E. coli*. Therefore, we chose Eyring's model, which has been verified for cationic leakage across the mitochondrial membrane (45) and that assumes $V(z)$ abruptly changes in the middle of the lipid bilayer such that $dV(z)/dz = 0$ everywhere but at the geometrical middle of the membrane, where $dV(z)/dz = V_m$ (46). We then have

$$k_{L,x} = \frac{S_{cell}}{V_{cell}} \times P_x \times [x]_{out} \times e^{-\frac{F \times V_m}{2 \times RT}}, \text{with } x \in \{Dye, C^+, A^-\}, \quad (9)$$

where $S_{cell}$ denotes the cell's surface area and $P_x$ the permeability of the membrane for $x \in \{Dye, C^+, A^-\}$ (obtained by assuming the solubility-diffusion model (47)).

At steady state, *Dye* and $A^-$ equilibrate across the membrane according to the Nernst equation ($d[Dye]_{in}/dt = j_{L,Dye} = 0 \Leftrightarrow \Delta G_{Dye} = 0$, leading to Eq. 2), whereas for the monovalent cation, $d[C^+]_i/dt = 0 \Leftrightarrow j_{L,C^+} = j_P$. Next, we introduce a new variable ("pump-leak ratio"), defined as

$$\rho = k_P / k_{L,C^+} = k_P \times \frac{V_{cell}}{S_{cell} \times P_{C^+} \times [C^+]_{out}} \times e^{\frac{F \times V_m}{2 \times RT}}, \quad (10)$$

and rewrite the steady-state condition for $C^+$ as

$$\left(1 - e^{\Delta G_{C^+}/(RT)}\right) = \rho \times \left(1 - e^{\left(\Delta G_E - \Delta G_{C^+}\right)/(RT)}\right). \quad (11)$$

Given a certain extracellular composition ($[Dye]_{out}$, $[C^+]_{out}$, and $[A^-]_{out}$) and taking into account that $[Dye]_{in}$ and $[A^-]_{in}$ are defined by the Nernst equation at steady state, Eq. 11 gives us a unique solution for steady-state $V_m$ for a set of $\{[Y]_{in}, \rho, \Delta G_E\}$ values while reducing the number of computational steps needed to reach it (see also the later paragraph describing computational steps of the model further).

We note from Eq. 11 that changing the functional dependency of $k_{L,C^+}$ or $k_P$ does not affect how the steady-state $V_{m,0}$ depends on $\rho$. However, the dynamics of dye equilibration and the steady-state potential after addition of the dye, relative to the steady-state potential in absence of the dye ($\Delta V_m = (V_{m,0} - V_{m,Dye})/V_{m,0}$), do. For example, had we assumed that the mechanism by which the ions leak across the *E. coli* membrane is better described by the Goldman-Hodgkin-Katz flux equation for $k_{L,x}$ (48), we would have obtained a slightly different dye equilibration profile (Fig. S3). However, the conclusions we reach based on our model predictions will not change because we are interested in the changes of the intracellular dye concentration dynamics at different extracellular dye concentrations, $V_{m,0}$ or $P_{Dye}$. These partial derivatives of the intracellular dye concentration are invariant to the choice of $k_{L,x}$ and $k_P$.

Having constructed the model, we obtain the computational data in Fig. 2 in two steps. In the first step, we allow the oridinary differential equation (ODE) system described by Eqs. S20 and S21 to reach the steady state ($V_{m,0}$) for a three-dimensional grid of $\{[Y]_{in}, \rho, \Delta G_E\}$. We note that in this step, we do not need to specify cation permeability nor the rate function for leakage $k_{L,C^+}$ because we define the values of $\rho$, which is the ratio of the two ($\rho = 0$ for the anion and the dye). We then use the obtained $V_{m,0}$ as the initial condition for the second step of the numerical experiment, which requires us to specify 1) the rate function for leakage (Eq. 9), 2) the permeability of the membrane to the dye $P_{Dye}$, and 3) the concentration of the dye in the extracellular space $[Dye]_{out}$, which does not affect the cation pumping rate in our model.

To explore the tradeoffs imposed on a Nernstian dye (Fig. 1), we first look at the choice of the working concentration. Increasing the [*Dye*] gives better signal/noise ratio but can affect $V_{m,0}$, as depicted in Fig. 2 *A*. For a fixed $V_{m,0}$, $[Y]_i$, and $\Delta G_E$, changing the external dye concentrations ($[Dye]_{out}$) improves the signal/noise ratio and shortens $\tau_{eq}$ but, at the same time, increasingly depolarizes the membrane. The extent by which $\Delta V_m$ drops does not solely depend on the $[Dye]_{out}$ but also on the initial $V_{m,0}$. Fig. 2 *B* shows dye equilibration profile for a fixed $[Dye]_{out}$ but for different $V_{m,0}$, indicating that highly polarized cells are more susceptible to $V_m$ loss. Apart from the value of $V_{m,0}$, $\Delta V_m$ will also depend on the charged permeable and nonpermeable species that are generating it, as shown in Fig. S4. If a given $V_{m,0}$ value is generated in the presence of a higher concentration of charged, impermeable intracellular species or at a higher energetic cost, $\Delta V_m$ will increase for the same $[Dye]_{out}$. Thus, the extent to which a given [*Dye*] becomes an actuator and affects the $\Delta V_m$ is context-dependent, and the dye working concentration should be determined for each specific physiological condition. Additionally, Fig. 2 *A* shows that increasing $[Dye]_{out}$ shortens $\tau_{eq}$, but only when $V_{m,0}$ is affected, as seen in Fig. S5.

Lastly, we look at the dye equilibration profile for different permeabilities of the membrane to the dye ($P_{Dye}$) in Fig. 2 *C* and show that for higher $P_{Dye}$, the same concentration of the dye lowers $V_{m,0}$ more. Fig. S4 shows $\tau_{eq}$ as a function of $P_{Dye}$ for different $V_{m,0}$.

## The working concentration of Nernstian dye ThT for *E. coli* is in μM range

Guided by the model predictions, we devise an experimental workflow for assessing the parametric range in which a candidate cationic dye behaves like an ideal Nernstian sensor. We choose ThT for the purpose; it has recently been used as a $V_m$ dye in *B. subtilis* (25), but it has not

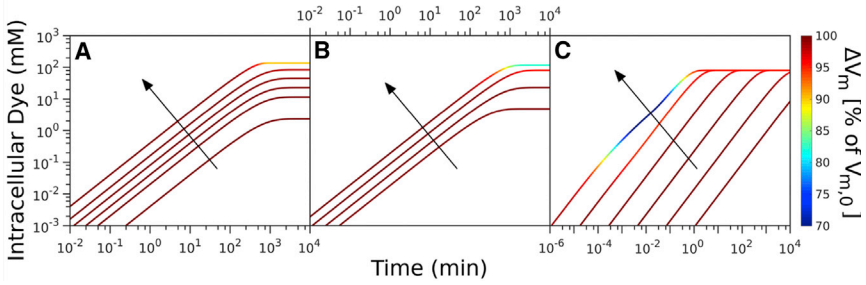


FIGURE 2 Computational data describing the parameter landscape associated with cationic dye usage as Nernstian sensors. (*A*) $V_{m,0} = -140$ mV, $Y_i = 150$ mM, $I_{Na} = 210$ mV. Intracellular dye concentration as a function of time is shown for extracellular dye concentrations 10, 50, 100, 200, 400, and 1000 $\mu$M. The arrow indicates increasing $[Dye]_{out}$. (*B*) Extracellular dye concentration of 100 $\mu$M is shown; $Y_i = 150$ mM, $\Delta G_E = -210$ mV. Intracellular dye concentration as a function of time is shown for different $V_{m,0}$: −220, −180, −140, and −100 mV. The arrow indicates increasing absolute value of the $V_{m,0}$. (*C*) Extracellular dye at 100 $\mu$M is shown; $V_{m,0} = -180$ mV, $Y_i = 150$ mM, $\Delta G_E = -210$ mV. Intracellular dye concentration as a function of time is shown for different apparent permeabilities of the membrane to the dye: $10^{-12}$, $10^{-10.8}$, $10^{-9.6}$, $10^{-8.4}$, $10^{-7.2}$, $10^{-6}$ m/s. The arrow indicates increasing permeability. To see this figure in color, go online.

been characterized for use in *E. coli*. We start by identifying the working concentration that gives sufficiently large signal yet minimizes the membrane voltage perturbation, $\Delta V_m$. Because we do not have access to $\Delta V_m$ directly, we grow the cells in the presence of ThT and use the growth rate as a proxy for affected $\Delta V_m$. We also know from our model predictions that $\Delta V_m$ is context-dependent, so we perform the experiment in two different media. Fig. 3, *A* and *B* show *E. coli* growth curves in MM9 media supplemented with glucose or glycerol, respectively (see Materials and Methods for detailed media composition), and in the presence of a range of ThT concentrations. To assess the effect of different ThT concentrations in these two media, we plot growth rates, obtained from growth curves in Fig. 3, *A* and *B*, against the ThT concentration. Fig. 3 *C* demonstrates that 10 $\mu$M ThT or less does not significantly affect the growth rate in either media, and we call this concentration the maximum noninhibitory concentration (MNC). The growth rate reduction we observe for higher ThT concentrations is media-dependent (Fig. 3 *C*). The result is consistent with the finding of our model that the effect of the dye on a cell's physiology is environment-dependent. It could be caused by a different $V_{m,0}$, difference in charged permeable and nonpermeable species that achieve the $V_{m,0}$, difference in the initial membrane permeability, or any combination of these factors.

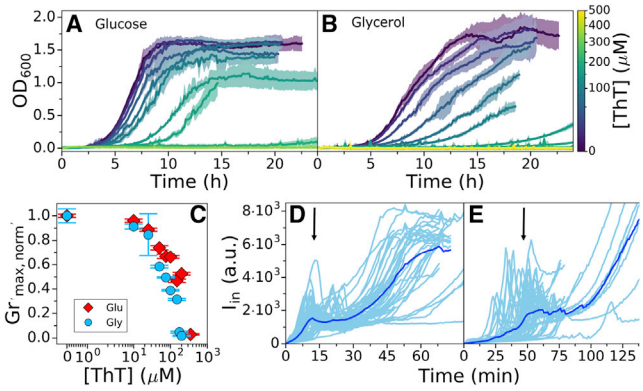


FIGURE 3 *E. coli* growth in the presence of ThT. *E. coli* growing in MM9 media supplemented with (*A*) glucose or (*B*) glycerol at increasing ThT concentration (*color map*) is shown. ThT concentrations in (*A*) are 10, 25, 50, 75, 100, 200, and 350 $\mu$M and in (*B*) are 10, 25, 50, 75, 100, 150, 175, and 200 $\mu$M. The error bars are standard deviations. (*C*) Maximum growth rates from (*A*) and (*B*) for each ThT concentration are given in red and blue, respectively. Each condition was done at least in triplicate, and error bars are the standard deviation. (*D*) $I_{in}$ against time in LB and in (*E*) MM9 + glucose media is shown. Individual cells are shown in cyan (45 in *D* and 52 in *E* from at least nine independent experiments), and the average trace is shown in blue. The imaging conditions and $I_{ex} = 10$ $\mu$M are the same for (*E*) and (*D*). The black arrows indicate the intensity peaks. To see this figure in color, go online.

We next check that the highest ThT concentration that does not affect the growth rate (MNC), 10 $\mu$M, gives sufficiently high signal/noise ratio by observing the dye equilibration in different media. For this purpose, we no longer grow the cells in the presence of ThT (see also Materials and Methods). We note that if sufficient $\Delta I$ is achieved with 10 $\mu$M ThT, we would further check that $\Delta V_m < 1\%$ by measuring the $\tau_{eq}$ with both 10 $\mu$M and a lower dye concentration. If $\Delta V_m < 1\%$, we expect $\tau_{eq}$ not to change based on the results of our model (Fig. 2 *A*). Fig. 3 *D* shows $I_{in}$ in time in LB, and Fig. 3 *E* shows the same in MM9 media supplemented with glucose. In both cases, fresh medium with ThT is continuously supplied using a customized flow cell (see Materials and Methods), and in both cases, $\Delta I$ is sufficiently high. However, observed profiles are different from expected (Fig. 1) and show a characteristic initial peak and a subsequent large increase that plateaus (Video S3). We reasoned that the peak could either be a real fluctuation in $V_m$ or it could indicate an unknown dye export mechanism.

## Deletion of the multidrug efflux pumps component TolC influences ThT dynamics in *E. coli*

To determine whether the observed peak in $I_{in}$ is due to active export of the dye, we first check that in *E. coli*, ThT is not a multidrug efflux pump substrate. We are motivated by previous reports that show dyes such as ethidium bromide and Nile red are substrates of pumps belonging to the five bacterial structural families: ATP-binding

cassette, resistance/nodulation/division, multidrug and toxic compound extrusion, major facilitator superfamily, and small multidrug resistance (49–53). Fig. 4 *A* shows dye equilibration curves in a WT strain compared to the strain bearing a deletion of TolC, which is a gene encoding for an outer membrane protein that is a ubiquitous component of multidrug efflux pumps (54). The $I_{in}$ peak in the deletion mutant did not disappear; instead, the intensity level of the peak was even higher, suggesting that the qualitative difference between the expected (Fig. 1) and the observed equilibration curve (Fig. 4 *A*) is not due to ThT export by TolC. Interestingly, in the mutant, the peak also occurred earlier in time during the loading and with less cell-to-cell variability. We next tested the effect of the ThT dye on the *ΔTolC* mutant growth rates, and for this purpose, we again grew the two strains in the presence of ThT (Fig. 4 *B*). We found that at the MNC for the WT, the mutants' growth was inhibited over the course of our experiment. Two different mechanisms could explain the results in Fig. 4: 1) ThT is a substrate of the multidrug efflux pumps or 2) membrane permeability of the TolC mutant is higher (55). In the first scenario, the strain lacking TolC accumulates more ThT than the WT (Fig. 4 *A*) and is therefore more affected by it (Fig. 4 *B*). In the second scenario, based on our model, we expect the intensity peak to appear earlier and at a higher $[Dye]_{in}$ (Fig. S12, *C* and *D*), which is what we observe in Fig. 4 *A*. We currently cannot distinguish between the two hypotheses, which could be contributing to the observed equilibration profiles at the same time.

## Changing the membrane permeability during ThT loading can lead to loss of $V_m$

We next tested our second hypothesis, that the $I_{in}$ peak is due to a decrease in $V_m$. To this end, we performed measurements of BFM speed (26) during ThT loading. The BFM is a rotary molecular motor roughly 50 nm in size that enables bacterial swimming (7) via PMF-driven rotation (56–59). The motor speed ($\omega$) varies linearly with PMF (59,60), which enables its use as a PMF indicator and, when $pH_{in} = pH_{out}$, as a $V_m$ indicator as well (26). In our conditions, $pH_{out}$ is 7 and $pH_{in}$ is 7.86 (Fig. S7), making the contribution to the PMF from $\Delta pH$ ~50 mV. Thus, even if during our experiment, $\Delta$pH goes to 0, we can learn about the $V_m$ behavior from the PMF measurements via the motor speed. We measure $\omega$ as before, using back-focal-plane interferometry (61) and a polystyrene bead attached to a short filament stub (see Materials and Methods) (26,30,62,63).

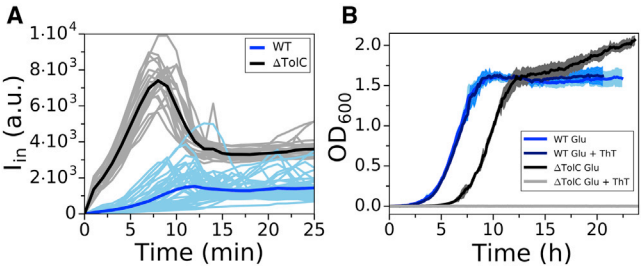


FIGURE 4 Comparison of WT and ΔTolC mutant response to ThT. (*A*) $I_{in}$ versus time for the WT (*cyan*) and ΔTolC (*gray*) loaded in LB is shown. WT traces are reproduced from Fig. 3 *D*, and ΔTolC traces were obtained from five independent experiments to give 23 single-cell traces. Averaged traces for the WT and ΔTolC are given in blue and black, respectively. (*B*) Growth curves of WT and ΔTolC in MM9 + glucose media are given in blue (reproduced from Fig. 3 *A*) and black, respectively. Growth curves in the same media, but in the presence of 10 μM ThT, are given in cyan (WT) and gray (ΔTolC). The shaded areas show standard deviation and cyan and blue growth curves for the WT overlap. To see this figure in color, go online.

Figs. 5 *A* and S8 show simultaneous measurements of ThT intensity and normalized motor speed during dye equilibration in MM9 + glucose. The motor speed decreases during ThT equilibration, and the BFM stops at the point of the $I_{in}$ peak. Furthermore, the BFM does not resume spinning even as $I_{in}$ further increases, suggesting that the second ThT intensity increase that culminates in a plateau is not driven by $V_m$. To confirm the result, during ThT equilibration, we supplemented the medium with PI. PI permeates bacterial membrane that lost its integrity and significantly enhances its quantum yield upon binding to DNA, which is commonly interpreted as an indication of cell death (64,65). We found that the cells stained with PI, although ThT intracellular concentration remained high (Figs. 5 *B* and S9). In addition, at the time point of $I_{in}$ decrease, cellular volume suddenly increases, and the cytoplasmically expressed fluorescent protein mCherry-mKate2 hybrid (referred to as mKate2 for brevity) (66) starts leaking out of the cell (Fig. 5 *C* and Video S4).

These results are in contradiction with our estimate of dye working concentration, and we wondered, based on Fig. 2 *C*, whether the changes in $P_{Dye}$ could be the explanation. The cell culture in Fig. 3 was briefly exposed to light at 600 nm every 7.5 min, whereas cells in our flow cell were exposed to light of 435 nm every minute for the purpose of imaging the ThT dye. We have previously reported loss of $V_m$ and PMF due to light-induced decrease of *E. coli* membrane's resistance at effective powers higher than ~17 mW/cm$^2$ and for a combination of 395 and 475 nm wavelengths (26). Light damage is wavelength-dependent (36), and we therefore characterized the light damage caused by our imaging conditions, i.e., 435 nm wavelength and effective power of $P_{eff}$ ~ 11 mW/cm$^2$. Fig. S10 shows a decrease in BFMs' speed and thus the cell's PMF. However, the PMF is not fully lost, indicating that the loss of PMF observed in Fig. 5 *A* is likely caused by the combination of light-induced increase in $P_{Dye}$ and exposure to 10 μM ThT.

To prove it, we exposed the bacteria to 10 μM ThT in LB as before, but this time, we observed the cells under bright-field illumination for 45 min, at which point we turned on

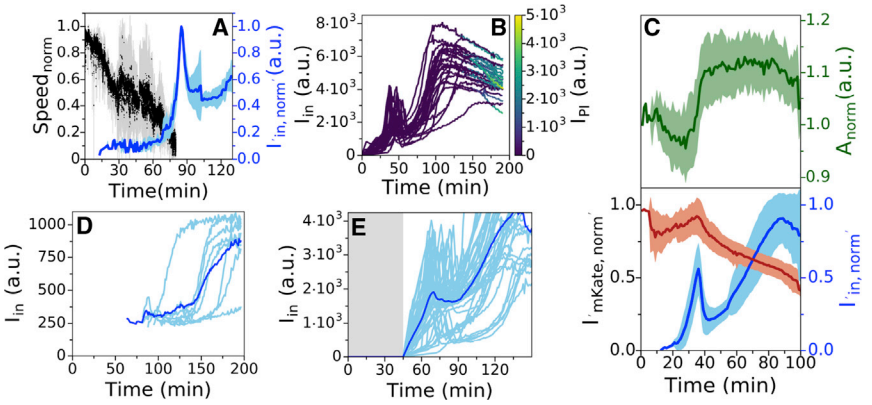


FIGURE 5 (*A*) Average traces of ThT fluorescence (in *blue*) and motor speed (in *black*) simultaneously measured in five individual cells (individual cell traces are given in Fig. S6). The shaded areas show the standard deviation, and the motor speed has been normalized to the initial value as described in Materials and Methods. (*B*) ThT (*y axes*) and PI (*color map*) equilibration profile in LB are shown. 25 individual traces are given. (*C*) Average of ThT (in *blue*), mKate2 (in *red*) fluorescence, and cell area (in *green*) simultaneously measured in 12 individual cells from three independent experiments is shown. The shaded areas show the standard deviation. (*D*) Equilibration profile of 1 $\mu$M ThT in LB is shown. Eight single-cell traces and average trace are given in cyan and blue, respectively. (*E*) Equilibration profile of 10 $\mu$M ThT in LB in the absence (*gray shaded area*) and presence of epifluorescent illumination (*light area*) is shown. The dye was flowed in the flow cell for the whole length of the experiment, and imaging conditions in the light area were the same as in Figs. 3 and 5 *D*. 44 cells from eight independent experiments are given. To see this figure in color, go online.

the 435 nm light used for epifluorescence imaging of ThT. Fig. 5 *E* shows that after 45 min, cells not exposed to 435 nm light did not take up ThT. This is in contrast to Fig. 3 *D*, in which cells exposed to 435 nm light from the start took up ThT in the first 30 min.

Actively changing membrane permeability has been used to facilitate loading of Nernstian sensors (21), and Fig. 5 *E* shows that this can change the dye into an actuator because it can influence $V_m$. Our mathematical model predicts that if a given concentration of the dye is lowering $V_m$, an even lower concentration of the dye will result in a change of $\tau_{eq}$ (Fig. S5). Because the dye equilibration profiles in Fig. 3 *D* do not follow the theoretically expected curve (Fig. 1), we cannot calculate $\tau_{eq}$. However, from Fig. 5 *A*, we know that initial rise in the dye intensity is still driven by $V_m$; therefore, we can qualitatively compare the timing of the initial rise at different $[Dye]_{out}$. Fig. 5 *D* shows that for 1 $\mu$M concentration of ThT, the rise in $I_{in}$ happens later in time than at $[Dye]_{out} = 10$ $\mu$M (Fig. 3 *D*). Thus, 10 $\mu$M ThT in LB under 435 nm light affects $V_m$. Assessing the suitability of the dye working concentration by confirming that a lower dye concentration does not alter $\tau_{eq}$ is a suitable additional control we propose, especially if $P_{Dye}$ is being altered as part of the experiments.

We note that in our plate reader experiments (Fig. 2), we observed the effect of the dye (above 10 $\mu$M) on cell growth, whereas in our microscopy experiments, in the absence of light damage, ThT does not permeate WT cells. We thus wanted to confirm that at higher concentrations, ThT permeates the cells on a longer timescale, and for this purpose, we imaged the cells from the wells at representative ThT concentrations in MM9 + glucose (10, 50, and 100 $\mu$M) and MM9 + glycerol (10 $\mu$M). As expected, we found that on a longer timescale in MM9 glucose, cell brightness increases with the extracellular dye concentration, and that in MM9 + glycerol, at 10 $\mu$M, ThT signal from the cells is overall greater than in glucose (Fig. S11).

Having identified the mechanisms behind the shape of the ThT loading curve we observed in Fig. 3, we should now be able to reproduce it with our mathematical model. We focus only on the part of the equilibration curve that is $V_m$-driven, i.e., up to the point $V_m$ drops to zero (as indicated in Fig. 5 *A*). Beyond, the increase in $I_{in}$ is not driven by a Nernstian equation and thus not accounted for in our model. Based on Fig. 5 *A*, we assume that $V_m$ decays exponentially immediately after addition of the dye (26): $V_m(t) = V_{m,0} \times 2^{t/t_{1/2}}$, where $t_{1/2}$ is the time at which voltage is half that of $V_{m,0}$. The dynamics of dye entry are then modeled by Eyring's rate law, Eq. 9, taking into account $V_{m,0}$, $t_{1/2}$, and $P_{Dye}$ (see Supporting Materials and Methods for further details on the model). Fig. S12 shows that the model reproduces the peak in $[Dye]_{in}$ observed in Fig. 3. Immediately upon addition, the positively charged dye moves inwards because its extracellular concentration is higher than the intracellular and the cell is negatively polarized. Thus, $[Dye]_{in}$ increases and becomes greater than $[Dye]_{out}$ until the electrochemical potential reaches $\Delta G_{Dye} = 0$ (at the peak). As the $V_m$ decays and because $[Dye]_{in} > [Dye]_{out}$, the dye now starts moving outwards, and its intracellular concentration decreases. In Fig. S12 *B*, $[Dye]_{\mathrm{in}}$ decreases to zero, whereas experimental $I_{in}$ starts increasing after the peak and never reaches zero. The difference is explained by the fact that cells with high $I_{in}$ after the peak are no longer viable (Fig. 5, *A* and *B*), and thus, the behavior of the dye is no longer governed with the Nernstian equation. In Fig. S12, *E* and *F*, we indicate the part of the experimental equilibration curve to which our model is applicable.

The time at which the peak occurs, as well as its intensity, depends on $P_{Dye}$ as follows: 1) the time of the peak decreases with increasing $P_{Dye}$ and increases with increasing $t_{1/2}$, and 2) the intensity of the peak increases with increasing $P_{Dye}$ and $t_{1/2}$ (Fig. S9, *C* and *D*). The dye still equilibrates according to Eq. 2; however, this is achieved transiently at the time of the peak, which is the time point

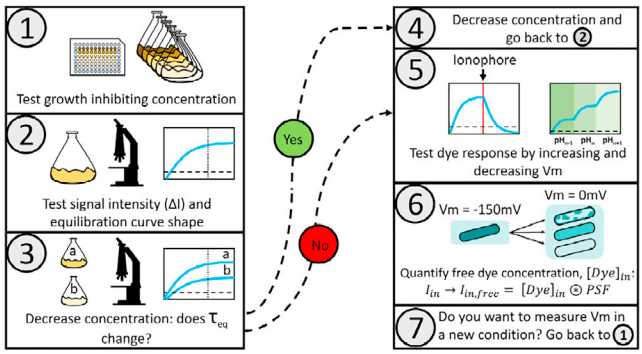


FIGURE 6 Proposed workflow for characterizing the Nernstian behavior of a candidate cationic membrane voltage dye. The working concentration is estimated in steps 1–4; we define it as the maximum dye concentration that does not affect membrane voltage and that yields sufficient amount of signal. 1) The MNC is estimated. 2) The MNC is tested for sufficient signal intensity and the shape of the equilibration profile is inspected. 3) The effect of the dye on $V_m$ is determined by measuring $\tau_{eq}$ at different below-MNC concentrations. 4) Different $\tau_{eq}$ for different dye concentrations indicate that the probe is altering $V_m$ and the working concentration should be reduced and the protocol resumed from step 2. Equal $\tau_{eq}$ indicates that the probe is not altering $V_m$. 5) Common procedures to test the expected Nernstian dye responses can then be applied, such as the introduction of a ionophore that neutralizes $V_m$ or changes in external pH that induce changes in $V_m$ (21). 6) $I_{in}$ from the free dye should be separated from the $I_{in}$ from the bound dye, and $[Dye]_{in}$ should be calculated from $I_{in}$ by taking into account the microscope's points spread function. 7) Because the effects depend on the physiological state of the cell, the procedure should be repeated for every experimental condition. To see this figure in color, go online.

at which $V_m$ can be calculated from Eq. 2. Because $V_m$ varies during the course of the experiment, the $V_m$ measured at the peak is not equal to $V_{m,0}$. Nonetheless, if we measure $V_m(t)/V_{m,0}$ as well as calculate the $V_m$ at the time of the peak using Eq. 2, in principle, we can estimate $V_{m,0}$ as well. Therefore, charged dyes can be used to estimate initial $V_m$ even in conditions in which they act as actuators and collapse $V_m$, if the dynamical shape of the $V_m$ loss is known.

## DISCUSSION

Nernstian probes are a popular choice for estimating bacterial $V_m$ because the concentration of the free dye directly depends on $V_m$ according to the Nernst equation. Despite the wide usage, the probes are often not sufficiently calibrated before use in different conditions. Here, we present a mathematical model that shows tradeoffs between requirements imposed on the dye: sufficient signal/noise ratio, sufficiently short dye equilibration time, and minimal effect on the cells' physiology. Based on the model results, we characterize in *E. coli* the fluorescent dye ThT, recently used in *B. subtilis* (25). Finally, we propose a general workflow for the characterization of Nernstian dye candidates (Fig. 6).

Results of our model show that the dye working concentration that does not affect $V_m$ is context-dependent, e.g., it can be different for different external media. The model also predicts that if $\Delta V_m = 0$ at a chosen dye working concentration, lower dye concentrations should leave $\tau_{eq}$ unchanged. The finding offers a simple test to confirm the suitability of the chosen dye working concentration.

For the case of *E. coli* and ThT as the candidate Nernstian dye, we experimentally find that the dye equilibration profile does not follow the theoretical expectation (Fig. 1). We test two possible explanations for the shape of the equilibration profile we observe in Fig. 2: 1) involvement of active efflux pumps and 2) significant $V_m$ decrease during ThT equilibration. Although we find that the strain lacking one of the efflux pumps shows a different equilibration profile when compared to the WT, it still does not behave as theoretically expected. Instead, we find that the permeability of *E. coli's* membrane to ThT is low. Permeabilizing the membrane by light of relatively short wavelengths to facilitate sufficient ThT entrance into the cell causes significant $V_m$ reduction, which subsequently results in cell death. The finding is consistent with previous results that show that *E. coli*'s membrane needs to be permeabilized with EDTA to achieve experimentally reasonable loading times of tetramethyl rhodamine methyl ester (TMRM) dye (21). EDTA is thought to increase the permeability of *E. coli* by chelating the metal ions that cross-link the lipopolysaccharide (LPS) (67). Some evidence also suggests that it might interact directly with lipids destabilizing the membrane (68). The equilibration profiles we observe for the efflux pump mutant strain can be explained either by the change in membrane permeability between the two strains or by active efflux.

We summarize the results from our model and experiments, as well as previous work on Nernstian $V_m$ dye usage, in a workflow (Fig. 6). We believe it is sufficiently simple and general to provide a common standard for benchmarking the cationic dye behavior and thus improve the robustness of $V_m$ measurements. It starts with a protocol to identify the dye working concentration (Fig. 6, *steps 1–4*). This is first carried out by assaying the effect of the dye on bacterial growth, as we did in Fig. 3, *A–C*, because it is a physiological variable that is easy to measure and it will likely be affected by changes in $V_m$ (*step 1*). In step 1, we identify the MNC as the maximum dye concentration that does not affect growth. We use it to measure the dye equilibration profile in step 2. This allows us not only to make sure that with the MNC, we are obtaining the expected shape of the equilibration profile, but also that the MNC gives sufficiently high intracellular signal. Next, we further test, as we did by comparing Figs. 3 *D* and 5 *D*, whether the MNC is affecting $V_m$ by checking that $\tau_{eq}$ for the MNC and a chosen concentration below it stay the same (*step 3*). If the below-MNC concentration and the MNC do not show the same $\tau_{eq}$, steps 1–3 need to be repeated for progressively lower dye concentrations until either the signal from the intracellular dye becomes too low or $\tau_{eq}$ does not differ between the two tested concentrations. In the second case, the higher concentration can be considered suitable. The next step in the workflow is more commonly performed when

assaying $V_m$ dyes (16,21), where cells' $V_m$ is changed in a known way, e.g., by exposing the cells to ionophores and observing $V_m$ collapse (*step 5*). Finally, quantifying $V_m$ requires estimation of $[Dye]_{in}$ from $I_{in}$ measurements, which can be done by distinguishing the free from the bound dye and by taking into account that the obtained $I_{in}$ is a convolution of $[Dye]_{in}$ and the microscope point spread function (21,23) (*step 6*). Because the dye's behavior is context-dependent, steps 1–6 should be repeated for each new experimental condition. Furthermore, if the dye fails any of the steps in the proposed workflow, it is not suitable for use as a Nernstian sensor. For example, ThT for the case of *E. coli* failed in steps 2 and 3, which is why we did not need to perform subsequent steps of the workflow.

## SUPPORTING MATERIAL

Supporting Material can be found online at https://doi.org/10.1016/j.bpj.2019.10.030.

## AUTHOR CONTRIBUTIONS

L.M., G.T., C.-J.L., F.B., and T.P. conceived the experiments and the computational work. L.M., T.T., Y.P., and Y.L. performed experiments. G.T. performed computational work. L.M. analyzed experimental data. L.M., G.T., C.-J.L., F.B., and T.P. interpreted the results and wrote the manuscript.

## ACKNOWLEDGMENTS

We thank Dario Miroli for help with image analysis, Nathan Lord and Sebastian Jaramillo-Riveri for donating us the construct containing the hybrid mCherry-mKate2 sequence, and Angela Dawson for retrieving the ΔTolC mutant from the Keio collection.

This work was financially supported by the Cunningham Trust scholarship ACC/KWF/PhD1 to T.P. and L.M.; the National Natural Science Foundation of China under grants No. 31722003 and No. 31770925 to F.B.; the Ministry of Science and Technology, Republic of China, under contract No. MOST-107-2112-M-008-025-MY3, to C.-J.L.; and Human Frontiers Program grant RGP0041/2015 to T.P., F.B., and C.-J.L. T.P. acknowledges the support of UK Research Councils Synthetic Biology for Growth programme and is a member of the Biotechnology and Biological Sciences Research Council/Engineering and Physical Sciences Research Council/Medical Research Council-funded Synthetic Biology Research Centre (BB/M018040/1).

## REFERENCES

1. Del Castillo, J., and B. Katz. 1954. Quantal components of the end-plate potential. *J. Physiol.* 124:560–573.
2. Mitchell, P. 1961. Coupling of phosphorylation to electron and hydrogen transfer by a chemi-osmotic type of mechanism. *Nature.* 191:144–148.
3. Ramos, S., and H. R. Kaback. 1977. The relationship between the electrochemical proton gradient and active transport in *Escherichia coli* membrane vesicles. *Biochemistry.* 16:854–859.
4. Bradbeer, C. 1993. The proton motive force drives the outer membrane transport of cobalamin in *Escherichia coli*. *J. Bacteriol.* 175:3146–3150.
5. Jahreis, K., E. F. Pimentel-Schmitt, …, F. Titgemeyer. 2008. Ins and outs of glucose transport systems in eubacteria. *FEMS Microbiol. Rev.* 32:891–907.
6. Wood, J. M. 2015. Bacterial responses to osmotic challenges. *J. Gen. Physiol.* 145:381–388.
7. Sowa, Y., and R. M. Berry. 2008. Bacterial flagellar motor. *Q. Rev. Biophys.* 41:103–132.
8. Strahl, H., and L. W. Hamoen. 2010. Membrane potential is important for bacterial cell division. *Proc. Natl. Acad. Sci. USA.* 107:12281–12286.
9. Bernstein, J. 1868. Ueber den zeitlichen verlauf der negativen schwankung des nervenstroms. *Pflügers Arch.* 1:173–207.
10. Hodgkin, A. L., and A. F. Huxley. 1939. Action potentials recorded from inside a nerve fibre. *Nature.* 144:710–711.
11. Neher, E., and B. Sakmann. 1976. Single-channel currents recorded from membrane of denervated frog muscle fibres. *Nature.* 260:799–802.
12. Sakmann, B., and E. Neher. 1984. Patch clamp techniques for studying ionic channels in excitable membranes. *Annu. Rev. Physiol.* 46:455–472.
13. Ling, G., and R. W. Gerard. 1949. The normal membrane potential of frog sartorius fibers. *J. Cell. Comp. Physiol.* 34:383–396.
14. Martinac, B., M. Buechner, …, C. Kung. 1987. Pressure-sensitive ion channel in *Escherichia coli*. *Proc. Natl. Acad. Sci. USA.* 84:2297–2301.
15. Martinac, B., P. R. Rohde, …, T. Nomura. 2013. Patch clamp electrophysiology for the study of bacterial ion channels in giant spheroplasts of E. coli. *Methods Mol. Biol.* 966:367–380.
16. Felle, H., J. S. Porter, …, H. R. Kaback. 1980. Quantitative measurements of membrane potential in *Escherichia coli*. *Biochemistry.* 19:3585–3590.
17. Tsutsui, H., S. Karasawa, …, A. Miyawaki. 2008. Improving membrane voltage measurements using FRET with new fluorescent proteins. *Nat. Methods.* 5:683–685.
18. Fluhler, E., V. G. Burnham, and L. M. Loew. 1985. Spectra, membrane binding, and potentiometric responses of new charge shift probes. *Biochemistry.* 24:5749–5755.
19. Kralj, J. M., D. R. Hochbaum, …, A. E. Cohen. 2011. Electrical spiking in *Escherichia coli* probed with a fluorescent voltage-indicating protein. *Science.* 333:345–348.
20. Sims, P. J., A. S. Waggoner, …, J. F. Hoffman. 1974. Studies on the mechanism by which cyanine dyes measure membrane potential in red blood cells and phosphatidylcholine vesicles. *Biochemistry.* 13:3315–3330.
21. Lo, C. J., M. C. Leake, …, R. M. Berry. 2007. Nonequivalence of membrane voltage and ion-gradient as driving forces for the bacterial flagellar motor at low load. *Biophys. J.* 93:294–302.
22. Kashket, E. R. 1985. The proton motive force in bacteria: a critical assessment of methods. *Annu. Rev. Microbiol.* 39:219–242.
23. Ehrenberg, B., V. Montana, …, L. M. Loew. 1988. Membrane potential can be determined in individual cells from the nernstian distribution of cationic dyes. *Biophys. J.* 53:785–794.
24. Te Winkel, J. D., D. A. Gray, …, H. Strahl. 2016. Analysis of antimicrobial-triggered membrane depolarization using voltage sensitive dyes. *Front. Cell Dev. Biol.* 4:29.
25. Prindle, A., J. Liu, …, G. M. Süel. 2015. Ion channels enable electrical communication in bacterial communities. *Nature.* 527:59–63.
26. Krasnopeeva, E., C. J. Lo, and T. Pilizota. 2019. Single-cell bacterial electrophysiology reveals mechanisms of stress-induced damage. *Biophys. J.* 116:2390–2399.
27. Baba, T., T. Ara, …, H. Mori. 2006. Construction of *Escherichia coli* K-12 in-frame, single-gene knockout mutants: the Keio collection. *Mol. Syst. Biol.* 2:2006.0008.
28. Datsenko, K. A., and B. L. Wanner. 2000. One-step inactivation of chromosomal genes in *Escherichia coli* K-12 using PCR products. *Proc. Natl. Acad. Sci. USA.* 97:6640–6645.

29. Pilizota, T., and J. W. Shaevitz. 2012. Fast, multiphase volume adaptation to hyperosmotic shock by *Escherichia coli*. *PLoS One.* 7:e35205.
30. Rosko, J., V. A. Martinez, …, T. Pilizota. 2017. Osmotaxis in *Escherichia coli* through changes in motor speed. *Proc. Natl. Acad. Sci. USA.* 114:E7969–E7976.
31. Rosko, J. 2017. Osmotaxis in Escherichia coli. University of Edinburgh, PhD thesis.
32. Krasnopeeva, E. 2019. Single cell measurements of bacterial physiology traits during exposure to an external stress. University of Edinburgh, PhD thesis.
33. Sulatskaya, A. I., A. V. Lavysh, …, K. K. Turoverov. 2017. Thioflavin T fluoresces as excimer in highly concentrated aqueous solutions and as monomer being incorporated in amyloid fibrils. *Sci. Rep.* 7:2146.
34. Maskevich, A. A., V. I. Stsiapura, …, K. K. Turoverov. 2007. Spectral properties of thioflavin T in solvents with different dielectric properties and in a fibril-incorporated form. *J. Proteome Res.* 6:1392–1401.
35. Maskevich, A. A., A. V. Lavysh, …, K. K. Turoverov. 2015. Spectral manifestations of thioflavin t aggregation. *J. Appl. Spectrosc.* 82:33–39.
36. Vermeulen, N., W. J. Keeler, …, K. T. Leung. 2008. The bactericidal effect of ultraviolet and visible light on Escherichia coli. *Biotechnol. Bioeng.* 99:550–556.
37. Buda, R., Y. Liu, …, T. Pilizota. 2016. Dynamics of *Escherichia coli*'s passive response to a sudden decrease in external osmolarity. *Proc. Natl. Acad. Sci. USA.* 113:E5838–E5846.
38. Wang, Y. K., E. Krasnopeeva, …, C.-J. Lo. 2019. Comparison of *Escherichia coli* surface attachment methods for single-cell, *in vivo* microscopy. *bioRxiv* https://doi.org/10.1101/648840.
39. Otsu, N. 1979. A threshold selection method from gray-level histograms. *IEEE Trans. Syst. Man Cybern.* 9:62–66.
40. Swain, P. S., K. Stevenson, …, T. Pilizota. 2016. Inferring time derivatives including cell growth rates using Gaussian processes. *Nat. Commun.* 7:13766.
41. Rybak, S. L., F. Lanni, and R. F. Murphy. 1997. Theoretical considerations on the role of membrane potential in the regulation of endosomal pH. *Biophys. J.* 73:674–687.
42. Grabe, M., and G. Oster. 2001. Regulation of organelle acidity. *J. Gen. Physiol.* 117:329–344.
43. Nelson, P. 2003. Biological Physics: Energy, Information, Life. W. H. Freeman, New York.
44. Keener, J., and J. Sneyd. 2009. Mathematical Physiology, Second Edition. Springer, Berlin, Germany.
45. Garlid, K. D., and P. Paucek. 2003. Mitochondrial potassium transport: the k(+) cycle. *Biochim. Biophys. Acta.* 1606:23–41.
46. Garlid, K. D., A. D. Beavis, and S. K. Ratkje. 1989. On the nature of ion leaks in energy-transducing membranes. *Biochim. Biophys. Acta.* 976:109–120.
47. Shinoda, W. 2016. Permeability across lipid membranes. *Biochim. Biophys. Acta.* 1858:2254–2265.
48. Goldman, D. E. 1943. Potential, impedance, and rectification in membranes. *J. Gen. Physiol.* 27:37–60.
49. Alvarez-Ortega, C., J. Olivares, and J. L. Martínez. 2013. RND multidrug efflux pumps: what are they good for? *Front. Microbiol.* 4:7.
50. Lubelski, J., W. N. Konings, and A. J. M. Driessen. 2007. Distribution and physiology of ABC-type transporters contributing to multidrug resistance in bacteria. *Microbiol. Mol. Biol. Rev.* 71:463–476.
51. Nikaido, H., and Y. Takatsuka. 2009. Mechanisms of RND multidrug efflux pumps. *Biochim. Biophys. Acta.* 1794:769–781.
52. Kuroda, T., and T. Tsuchiya. 2009. Multidrug efflux transporters in the MATE family. *Biochim. Biophys. Acta.* 1794:763–768, Published online December 6, 2008.
53. Bay, D. C., K. L. Rommens, and R. J. Turner. 2008. Small multidrug resistance proteins: a multidrug transporter family that continues to grow. *Biochim. Biophys. Acta.* 1778:1814–1838.
54. Anes, J., M. P. McCusker, …, M. Martins. 2015. The ins and outs of RND efflux pumps in *Escherichia coli*. *Front. Microbiol.* 6:587.
55. Dhamdhere, G., and H. I. Zgurskaya. 2010. Metabolic shutdown in *Escherichia coli* cells lacking the outer membrane channel TolC. *Mol. Microbiol.* 77:743–754.
56. Manson, M. D., P. M. Tedesco, and H. C. Berg. 1980. Energetics of flagellar rotation in bacteria. *J. Mol. Biol.* 138:541–561.
57. Matsura, S., J. Shioi, and Y. Imae. 1977. Motility in Bacillus subtilis driven by an artificial protonmotive force. *FEBS Lett.* 82:187–190.
58. Meister, M., and H. C. Berg. 1987. The stall torque of the bacterial flagellar motor. *Biophys. J.* 52:413–419.
59. Fung, D. C., and H. C. Berg. 1995. Powering the flagellar motor of Escherichia coli with an external voltage source. *Nature.* 375:809–812.
60. Gabel, C. V., and H. C. Berg. 2003. The speed of the flagellar rotary motor of *Escherichia coli* varies linearly with protonmotive force. *Proc. Natl. Acad. Sci. USA.* 100:8748–8751.
61. Svoboda, K., C. F. Schmidt, …, S. M. Block. 1993. Direct observation of kinesin stepping by optical trapping interferometry. *Nature.* 365:721–727.
62. Ryu, W. S., R. M. Berry, and H. C. Berg. 2000. Torque-generating units of the flagellar motor of *Escherichia coli* have a high duty ratio. *Nature.* 403:444–447.
63. Bai, F., R. W. Branch, …, R. M. Berry. 2010. Conformational spread as a mechanism for cooperativity in the bacterial flagellar switch. *Science.* 327:685–689.
64. López-Amorós, R., J. Comas, and J. Vives-Rego. 1995. Flow cytometric assessment of *Escherichia coli* and *Salmonella typhimurium* starvation-survival in seawater using rhodamine 123, propidium iodide, and oxonol. *Appl. Environ. Microbiol.* 61:2521–2526.
65. Krämer, C. E., W. Wiechert, and D. Kohlheyer. 2016. Time-resolved, single-cell analysis of induced and programmed cell death via non-invasive propidium iodide and counterstain perfusion. *Sci. Rep.* 6:32104.
66. Lord, N. D. 2014. Fluctuation timescales in bacterial gene expression. Harvard University, PhD thesis.
67. Vaara, M. 1992. Agents that increase the permeability of the outer membrane. *Microbiol. Rev.* 56:395–411.
68. Prachayasittikul, V., C. Isarankura-Na-Ayudhya, …, H. J. Galla. 2007. EDTA-induced membrane fluidization and destabilization: biophysical studies on artificial lipid membranes. *Acta Biochim. Biophys. Sin. (Shanghai).* 39:901–913.

**Biophysical Journal, Volume *117***

## Supplemental Information

# A General Workflow for Characterization of Nernstian Dyes and Their Effects on Bacterial Physiology

**Leonardo Mancini, Guillaume Terradot, Tian Tian, YingYing Pu, Yingxing Li, Chien-Jung Lo, Fan Bai, and Teuta Pilizota**

# A general work-flow for the characterization of Nernstian dye candidates and their effects on bacterial physiology

**L Mancini[1], G Terradot[1,*], T Tian[2,*], Y Pu[2], Y Li[2], CJ Lo[3], F Bai[2], and T Pilizota[1,+]**

[*]**these authors contributed equally to this work**
[+]**Corresponding author:teuta.pilizota@ed.ac.uk**

## SUPPLEMENTARY FIGURES

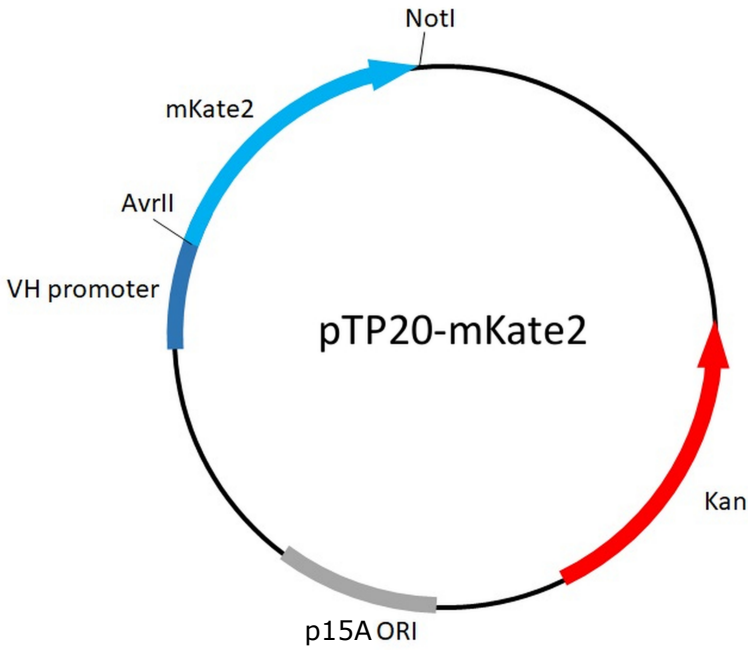


**Supplementary figure 1.** Plasmid map of pTP20-mKate2 showing the insertion site of mCherry-mKate2 hybrid (mKate2 for brevity) [1]. The constitutive cytochrome oxidase promoter from *Vibrio Harveyi* [2], the origin of replication and the Kanamycin resistance cassette are indicated.

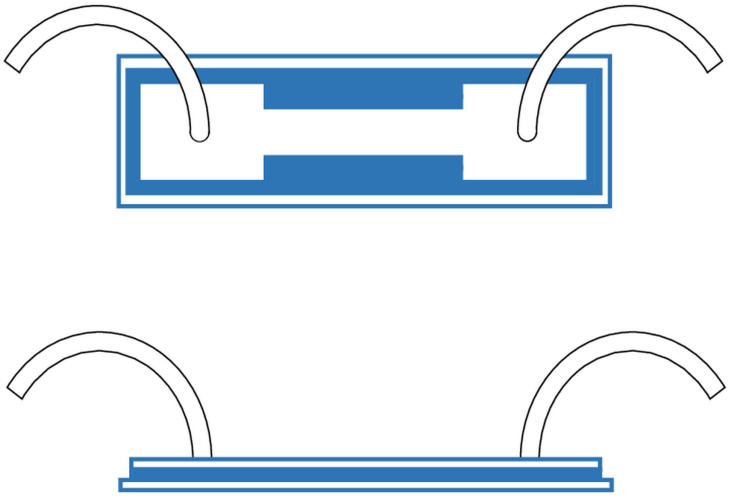

**Supplementary figure 2.** Schematic of our flow-cell. Microscope slide and coverslip are held together by custom cut Gene Frames (Thermo Fisher Scientific, UK). To exchange liquids, we drill two holes on the microscope slide and attach tubing using epoxy glue on the outside of the slide [3].

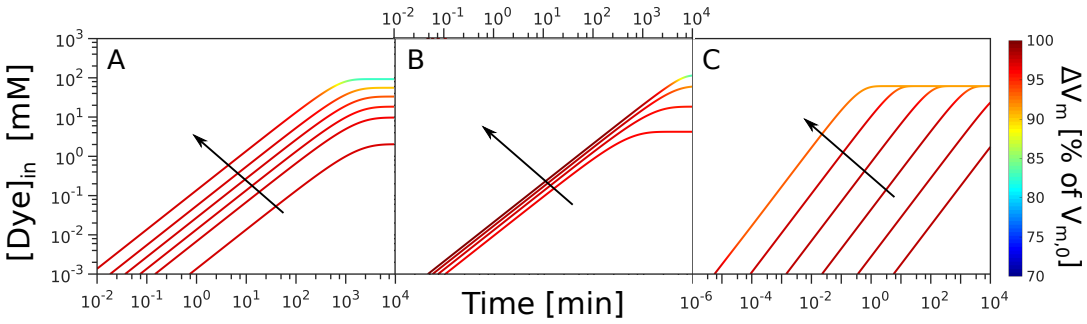


**Supplementary figure 3.** Dynamics of the dye loading assuming GHK rate law for leakage (Eq. (14)), where we assumed Eyring rate (law Eq. (13)) in Fig. 2 of the main text. (A) Intracellular Dye concentration as a function of time, for extracellular dye concentrations 10, 50, 100, 200, 400 and 1000 $\mu$M. The arrow indicated increasing $[Dye]_{out}$, and $V_{m,0} = -140$ mV, $Y_i = 150$ mM, $\Delta G_E = -210$ mV. (B) Intracellular dye concentration as a function of time for different $V_{m,0}$: $-220$, $-180$, $-140$ and $-100$ mV. The arrow indicates increasing absolute value of the $V_{m,0}$, and $[Dye]_{out} = 100$ $\mu$M, $Y_i = 150$ mM and $\Delta G_E = -210$ mV. (C) Intracellular dye concentration as a function of time for different apparent permeabilities of the membrane (with respect to the dye): $10^{-12}$, $10^{-10.8}$, $10^{-9.6}$, $10^{-8.4}$, $10^{-7.2}$, $10^{-6}$ m/s. The arrow indicates increasing permeability, and $V_{m,0} = -180$ mV, $Y_i = 150$ mM, $\Delta G_E = -210$ mV and $[Dye]_{out} = 100$ $\mu$M.

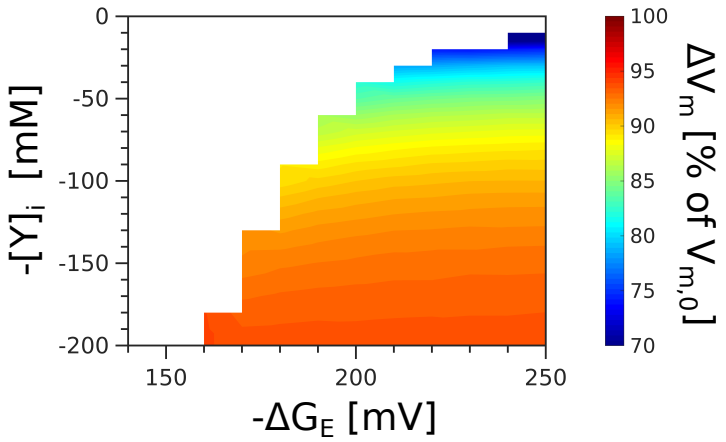


**Supplementary figure 4.** $\Delta V_m$ depends on the free energy available for transport of $[C^+]$ as well as on the contribution of charged impermeable species ($[Y_i]$), even for the same value of $V_{m,0}$. $[Dye]_{out} = 100\ \mu$M. $V_{m,0} = -180$ mV. Colour scale on the right gives $\Delta V_m$ values.

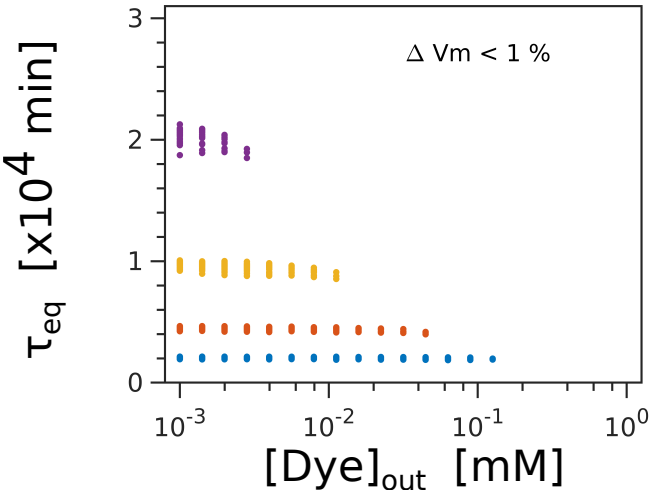


**Supplementary figure 5.** Equilibration time, $\tau_{eq}$, as a function of $[Dye]_{out}$ for different $V_{m,0}$ values. The permeability of the dye was set to $P_{Dye} = 10^{-10}$ m/s. Purple, yellow, red and blue are $V_{m,0}$ of $-220$, $-180$, $-140$ and $-100$ mV ($\pm 5$ mV), respectively. For each value of $[Dye]_{out}$ we plot all the values of $\tau_{eq}$ that yield the desired $V_{m,0} \pm 5$ mV, where $\{[Y]_{in}, \rho, \Delta G_E\}$ were varied in the range specified in Table 4. The simulations that change $V_{m,0}$ by less than 1% mV are plotted, showing that when $\Delta V_m \sim 0$, $\tau_{eq}$ is a function of $V_{m,0}$ only.

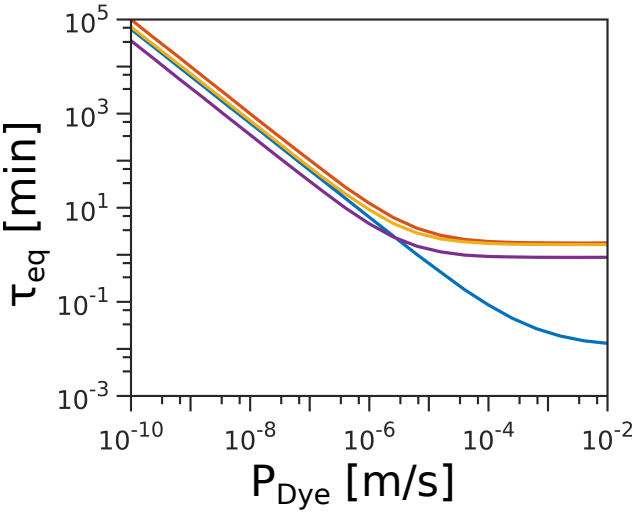


**Supplementary figure 6.** Equilibration time, $\tau_{eq}$, as a function of the dye permeability. The following were set: $[Y]_i = 150$ mM, $\Delta G_E = -210$ mV, $[Dye]_{in} = 100$ $\mu$M. The blue, red, yellow and purple lines are for $V_{m,0}$ of $-220$, $-180$, $-140$ and $-100$ mV, respectively. For each of them, $\Delta V_m$ is permeability invariant and takes the respective values of 83%, 93%, 96% and 97%.

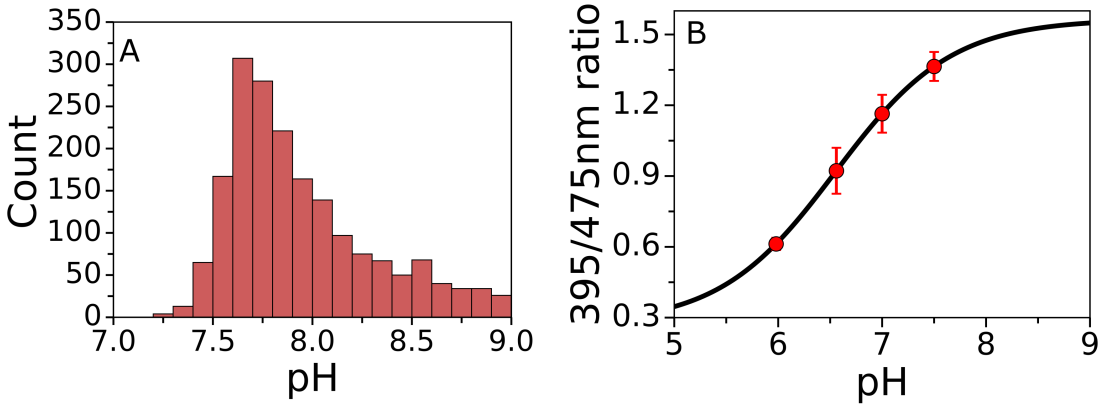


**Supplementary figure 7.** Intracellular pH measurements. (A) Using chromosomally expressed pHluorin [3, 4] we measure intracellular pH in 2346 individual cells. The median value of the distribution is 7.86. (B) *In vivo* pHluorin calibration curve where the cells were exposed to 40 mM potassium benzoate and 40mM methylamine hydrochloride in order to collapse internal pH [4]. Data points are an average of $\sim$400 cells and error bars give the standard deviation.

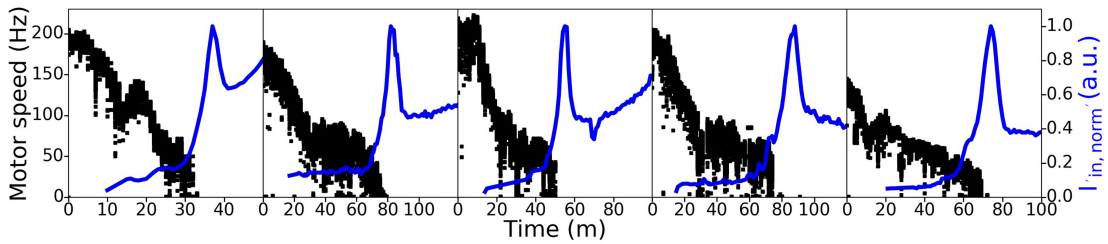


**Supplementary figure 8.** Individual motor traces (black) that were averaged in Fig. 5A. ThT intensity traces are given in blue, and imaging and exposure setting are as specified in *Material and Methods*.

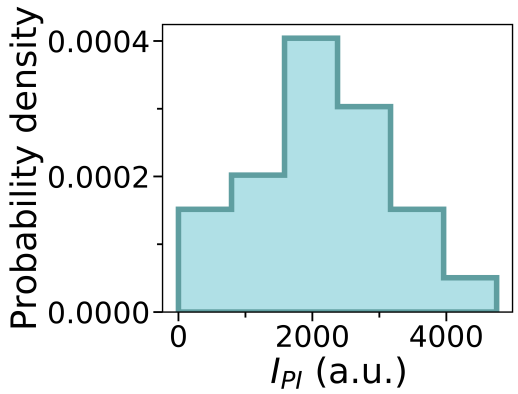


**Supplementary figure 9.** Probability density function of the final intensity values of propidium iodide from Fig. 5B ($I(t_f)$ with $t_f$ = 185 min). Cell count is 25 from 3 different experiments.

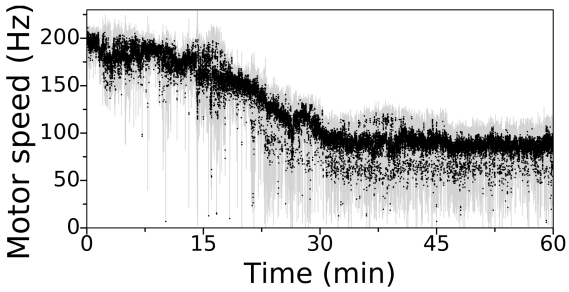


**Supplementary figure 10.** Light-induced damage quantified by measuring PMF loss via bacterial flagellar motor speed, over the length of an hour. The experiment was carried out as in Fig. 5A, but ThT was not added to the MM9 + glucose media, which was continuously supplied through out the experiment with a flow rate of 50 $\mu$l/min. Black shows the average of three individual motor speed recordings, each on a different cell, and grey area shows the standard deviation.

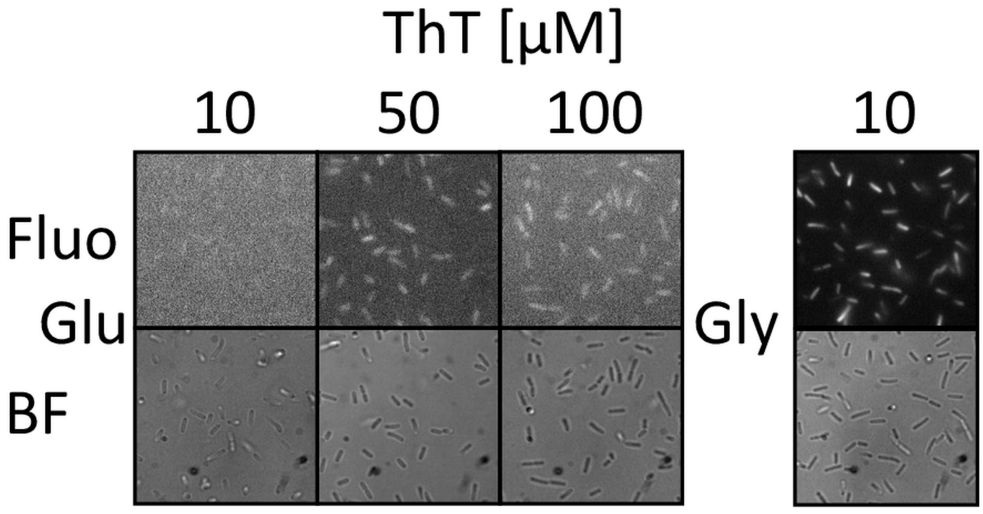


**Supplementary figure 11.** Cells grown in the plate reader (Fig 3A, B and C) in the presence of ThT were imaged, in order to estimate the extent of dye equilibration. "Fluo" abbreviation indicates fluorescence intensity and "BF", the brightfield image. Imaging conditions for ThT are the same as those used throughout the paper (Fig.3D E, 4A, 5A, B, C D). Cells were imaged after 7 h of growth in the plate reader (OD= 0.5- 0.6 when grown on glucose and 0.4 on glycerol) when 10 and 50 $\mu$M ThT was present, and after 8.5 h (OD 0.7 when grown on glucose) for the 100 $\mu$M ThT case.

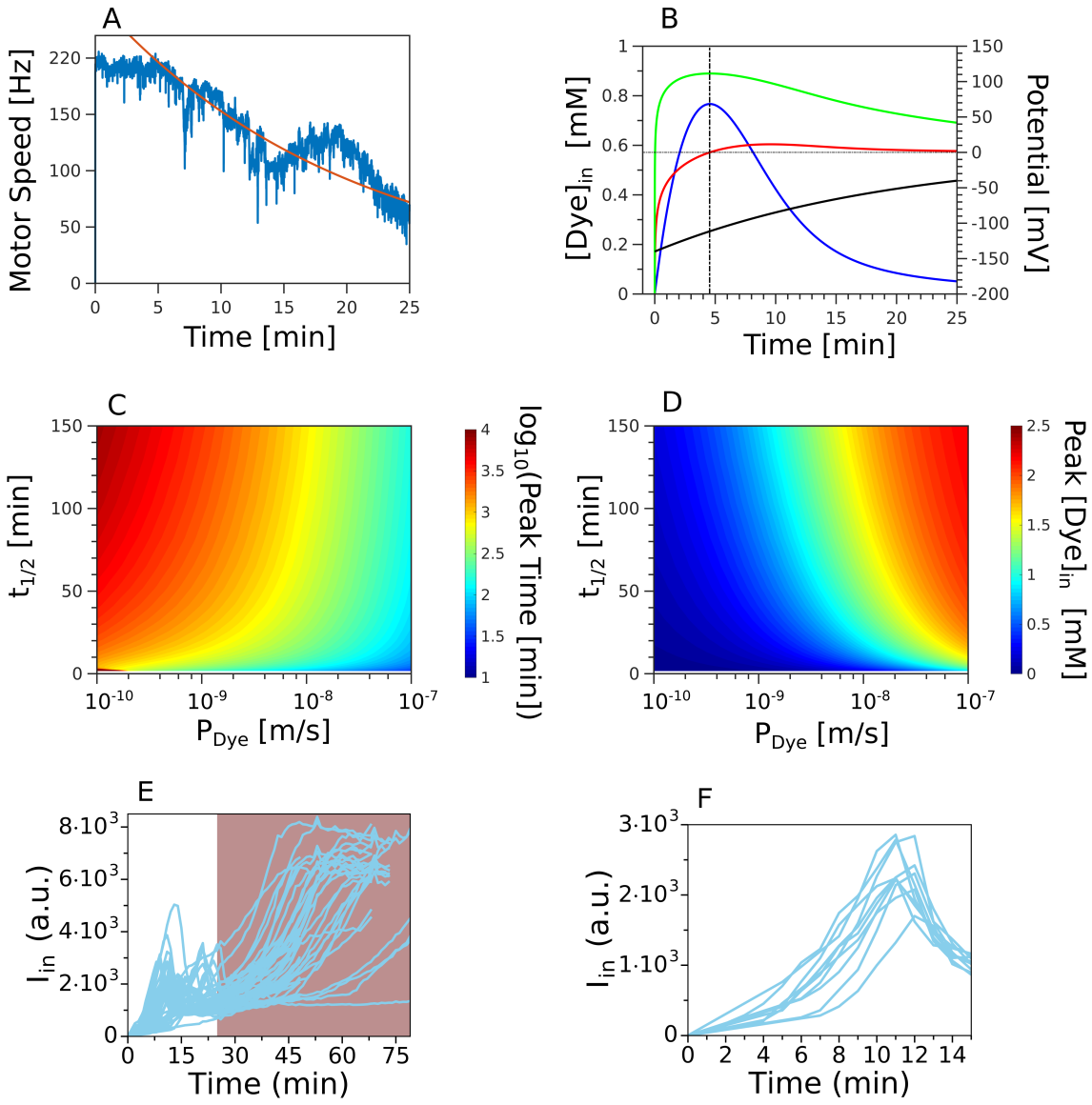


**Supplementary figure 12.** (A) Exponential decay of $V_m$ during ThT loading leads to an intensity peak. Exponential fit (in red and starting from the time we observe the decay) to the first motor speed trace shown in Fig. SI5. The half-time of the decay is $t_{1/2} = 16.4$ min, which we use as the decay time of $V_m$. (B) Dye equilibration profile for the case of exponentially decaying $V_m$ (black) is plotted in blue. The permeability of the dye was set to $P_{Dye} = 10^{-8}$ m/s, $[Dye]_{out} = 10^{-2}$ mM, and $V_{m,0} = -140$ mV. Green line depicts the contribution of the concentration gradient to the dye electrochemical potential $\ln([Dye]_{in}/[Dye]_{out})$ and red line the electrochemical potential of the dye. (C) Peak time (in log scale) and (D) peak intracellular dye concentration as a function of $t_{1/2}$ and the dye permeability. For both (C) and (D) we assumed $V_{m,0} = -140$ mV. (E) The model is relevant for the part of the equilibration profile that is driven by $V_m$. Subsequent increase in ThT intensity (shaded in red) does not obey Nernstian equation, because $V_m$ is zero (Fig. 5A) and cell membrane is compromised (Fig. 5B). The traces are reproduced from Fig. 3D. (F) 10 example traces from Fig. 3D showing the portion of the equilibration curve described by our model.

## SUPPLEMENTARY VIDEOS

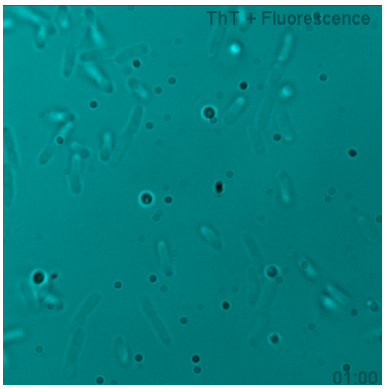


**Supplementary video 1.** *E. coli* growing in LB medium in our flow cell before addition of the ThT dye (images shown in gray-scale). In yellow we colour the frames that correspond to addition of the dye but without epifluorescence imaging. While the dye is present in the medium, it does not enter the cytoplasm, and thus the cells continue to grow. We colour in cyan the frames where both the ThT and epifluorescence imaging is happening at the same time. ThT now enters the cytoplasm and cells stop growing. The brightfield images correspond to one of the experiments presented in Fig. 5E.

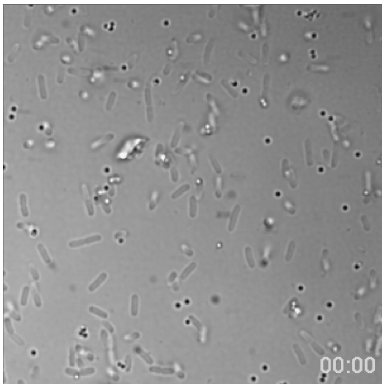


**Supplementary video 2.** Growth of *E. coli* in our flow cell, in MM9 + glucose medium, in the presence of epifluorescence illumination. The brightfield images are from one of the experiments in Fig. SI10. Cells grow in our flow cell when epifluorescence imaging is turned on.

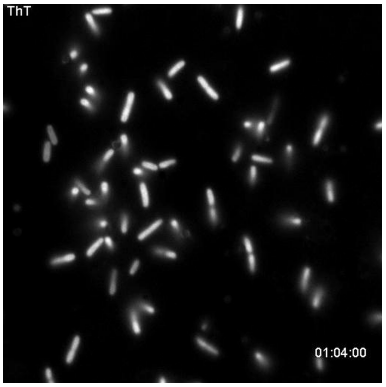


**Supplementary video 3.** Equilibration of ThT in LB. Dynamics of ThT equilibration in a flow slide in LB medium from the experiments in Fig. 3D. Images are taken every minute.


**Supplementary video 4.** Characteristic single cell volume change and cytoplasmic marker loss during ThT equilibration. Dynamics of cytoplasmic mKate2 fluorescent signal (right) during ThT equilibration (left) from the experiment in Fig. 5 C. Images are taken every minute.

## SUPPLEMENTARY TABLES

| Plasmid | Fragment | Primers |
|---|---|---|
| pTP20-mKate2 | pWR20 backbone [2] | 5' AAAGCGGCCGCGGTGATTGATTGAGCAAG 3'<br>5' AAACCTAGGATGTATATCTCCTTAACTAGGT 3' |
| pTP20-mKate2 | mCherry-mKate2 hybrid [1] | 5' AATGCGGCCGCTTATCTGTGCCCCAGTTT 3'<br>5' ATACCTAGGATGGTTAGTAAAGGAGAAGAA 3' |

**Table 1.** Plasmids and primers used in this work.

| Strain | Origin | Figure |
|---|---|---|
| MG1655 | | 3, 4A, 5B, 5E, 5D and SI 2, 9 |
| MG1655-*pTP20-mKate2* | This work | 5C |
| EK01 | [3] | 5A and SI 4,5,7 |
| EK07 | [3] | SI 10 |
| BW25113 Δ*tolC* pTP20-mKate2 | This work | 4A, 4B |

**Table 2.** List of *E. coli* strains used in this work.

| Name | Symbol | Value | Units | Reference |
|---|---|---|---|---|
| Faraday constant | $F$ | 96485 | C/mol | |
| Gas constant | $R$ | 8.31 | J/mol/K | |
| Temperature | $T$ | 298 | K | |
| Avogadro Number | $N_A$ | $6.02 \times 10^{23}$ | $\text{mol}^{-1}$ | |
| Cell length | $l_{cell}$ | $2.95 \times 10^{-6}$ | m | [5] |
| Cell width | $w_{cell}$ | $1.07 \times 10^{-6}$ | m | [5] |
| Cell surface | $S_{cell}$ | $9.91 \times 10^{-12}$ | $\text{m}^2$ | Eq. SI(3) |
| Cell volume | $V_{cell}$ | $2.33 \times 10^{-18}$ | $\text{m}^3$ | Eq. SI(4) |
| Membrane Specific Capacitance | $C_m$ | $6.5 \times 10^{-3}$ | $\text{F/m}^2$ | [6] |
| Total Membrane Capacitance | $C$ | $6.45 \times 10^{-14}$ | F | Eq. SI(2) |
| Total Extracellular ionic concentration | $\Pi_e$ | 200 | $\text{mol/m}^3$ | |
| Membrane Permeability to $C^+$ | $P_{C^+}$ | $1.8 \times 10^{-9}$ | m/s | [7] ($K^+$) |
| Membrane Permeability to $A^-$ | $P_{A^-}$ | $1.4 \times 10^{-10}$ | m/s | [7] ($Cl^-$) |

**Table 3.** Parameters used for the simulations. The cell length and width in MM9+glucose were obtained from our fluorescence microscopy measurements and are consistent with [5].

| Sampled parameters | Range of values | Spacing | Number of values |
|---|---|---|---|
| $\Delta G_E$ | $-250\text{mV} \leq \Delta G_E/F \times 10^{-3} \leq -50\text{mV}$ | Linear | 21 |
| $[Y]_{in}$ | $0 \leq [Y]_{in} \leq 200$ Moles/meter$^3$ | Linear | 21 |
| $\rho$ | $10^{-4} \leq \rho \leq 10^5$ | $\log_{10}$ | 1000 |

**Table 4.** Value of parameters used when solving Eqs. SI 20 and 21 to obtain $V_{m,0}$.

# SUPPLEMENTARY TEXT

## Supplementary methods

### *Intracellular pH estimation.*

To estimate the intracellular pH we used *EK07* cells grown to OD 0.8 in TB at 30°C and transferred to MM9 + glucose media, as for the experiments in Fig. 5A and as in [8]. Imaging was carried out in a flow-cell with a 50 ms exposure time and gain set to 300. Illumination at 395 nm and 470 nm was provided by a narrow spectrum UV LED and a Neutral White LED (Cairn Research Ltd, UK), respectively [3]. The filters used were ET470/40x and ET525/40m (Chroma Technology, USA) for the excitation at 470 nm and the emission of both [3]. The *in vivo* calibration curve of *EK07* cells expressing pHluorin was obtained by collapsing cytoplasmic pH using 40 mM potassium benzoate and 40 mM methylamine hydrochloride [9]. The mixture was added to MM9 + glucose media and the pH of the solution was adjusted to 5.98, 6.56, 7 or 7.5, respectively. The media at different pH were introduced into the flow-cell and imaging was carried out 5 min after [10]. Data was fitted to a sigmoid: $R395/475 = \frac{a_1 e^{k(pH-pH_0)} + a_2}{e^{k(pH-pH_0)} + 1}$ where $a_1$, $a_2$, k and $pH_0$ are fitting parameters as in [3] ($a_1$ = 1.56449665, $a_2$ = 0.27090295, k = 1.79203546 and $pH_0$ = 6.55202883).

## Detailed description of the model

As mentioned in the main text we treat the *E. coli's* membrane as a parallel-plate capacitor and write the $V_m$ as [11]:

$$V_m = F \cdot \frac{Q_{in}}{C} \tag{1}$$

where $Q_{in}$ is the intracellular total charge (in mole) and $C$ the membrane capacitance that depends on the membrane specific capacitance and the cell's surface area:

$$C = S_{cell} \cdot C_m \tag{2}$$

To calculate $S_{cell}$ we assume the cell is a spherocylinder with 3:1 length to width ratio (determined from our microscopy images and consistent with [5]) and write as in [12]:

$$S_{cell} = \pi w_{cell} \cdot l_{cell} \tag{3}$$

$$V_{cell} = \pi \left(\frac{w_{cell}}{2}\right)^2 \left(l_{cell} - \frac{w_{cell}}{3}\right) \tag{4}$$

where $l_{cell}$, $w_{cell}$ and $V_{cell}$ are cell length, width and volume respectively.

Equation (3) in the main text lists the ionic species that contribute to $Q_{in}$ and we assume electroneutrality in the extracellular space such that:

$$[C^+]_{out} - [A^-]_{out} + [Dye]_{out} = 0 \tag{5}$$

We keep the total ionic concentration in the extracellular medium, $\Pi_e$, fixed in the simulations:

$$[C^+]_{out} + [A^-]_{out} + [Dye]_{out} = \Pi_e \tag{6}$$

Consequently from SI Eqs. (5) and (6), the ionic composition of the medium only depends on the choice of $[Dye]_{out}$ and follows:

$$[C^+]_{out} = \frac{\Pi_e}{2} - [Dye]_{out} \tag{7}$$

$$[A^-]_{out} = \frac{\Pi_e}{2} \tag{8}$$

Separation of charges, and thus $V_m$, is governed by two type of reactions: leakage and active pumping, which means that the intracellular concentration of charged species we consider, changes in time as follows:

$$\frac{d[A^-]_{in}}{dt} = j_{L,A^-} \tag{9}$$

$$\frac{d[Dye]_{in}}{dt} = j_{L,Dye} \tag{10}$$

$$\frac{d[C^+]_{in}}{dt} = j_{L,C^+} - j_P \tag{11}$$

where equations (4) and (7) in the main text give reaction rates $j_{L,x}$, $j_P$, respectively. Given that chemical species $Y$ cannot cross the membrane, $Y$ contributes to $Q_{in}$ in time invariant manner determined by the initial conditions only. $k_{L,x}$, $k_P$ in the equations (4) and (7) in the main text describe the detailed mechanism by which ions leak or are pumped across the biological membrane. In the main text we mentioned we chose $k_P$ to be a constant and $k_{L,x}$ we base on Eyring's model [13] (equation (9) of the main text).

Choosing the forward rate of pumping $k_P$ to be a constant implies the choice of a reversible rate function that describes at least a 2-step reaction operating always in the saturating regime for all its input variables (substrate/product concentrations and voltage), *i.e.* we assume $k_P \approx N_{Pump} \cdot v_{max}$ where $N_{Pump}$ is the number of pumps and $v_{max}$ the maximum rate per pump. In general, $k_P$ is expected to depend on the input variables, and one can derive the specific functional dependency if one assumes a particular mechanism of action for the pump. To do so, we would also need to specify additional parameters characteristic for a given pump, such as affinities for its substrate, dependency on $V_m$, etc. This is out of the scope of this work, where we model a generic pump, and we refer the reader to [14] to find some examples of other rate laws for electrogenic pumps.

Eyring's model for $k_{L,x}$ is a special case of the so-called trapezoidal energy barrier model, which is a general model for describing the dynamics of ionic leakage across the membrane and is given as

$$j_{L,x} = \frac{S_{cell}}{V_{cell}} P_x \cdot b \cdot u \frac{[x]_{out} \cdot e^{u/2} - [x]_{in} \cdot e^{-u/2}}{e^{bu/2} - e^{-bu/2}} \tag{12}$$

where $u = -\frac{F}{RT} \cdot V_m$, $P_x$ the so-called apparent permeability of the membrane for species $x$, and $b$ is the so-called fractional width of the trapezoid. The SI Eq. (12) is the Eq. 7 in [13], which we multiply by $\frac{S_{cell}}{V_{cell}}$ to have the flux in units mole/volume/time rather than mole/surface/time, and which was first derived in [15, 16].

The apparent permeability is defined as: $P_x = \overline{P}_x \cdot \frac{[x]_{out}^{(interface)}}{[x]_{out}^{(bulk)}}$ where $\overline{P}_x$ is the specific permeability of the membrane for $x$ and $[x]_{out}^{(interface)}$, $[x]_{out}^{(bulk)}$ are respectively the concentrations of $x$ at the interface of the membrane and in the bulk (far away from the membrane). When $V_m = 0$ we expect $[x]_{out}^{(interface)} = [x]_{out}^{(bulk)}$ and the apparent and specific permeabilities to be identical. When $V_m \neq 0$ the ionic concentrations at the membrane is different compared to the bulk, ordinarily positive at the extracellular and negative at the intracellular interface, which can influence the *apparent* membrane permeability (see section 4 of [17] for more details).

In Eq. (12) $b$ is parameter that characterizes the shape of the voltage drop across the membrane ($0 \leq b \leq 1$). More specifically, $b$ characterizes $\frac{dV(z)}{dz}$ where $z$ denote the position within the membrane. If $b = 0$, $V(z)$ abruptly changes in the middle of the lipid bilayer such that $\frac{dV(z)}{dz} = 0$ everywhere but at the geometrical middle of the membrane. This is known as the single Eyring barrier assumption and taking into the account the equation for the electrochemical potential (8) given in the main text, it reduces the SI Eq. (12) to:

$$j_{L,x} = \frac{S_{cell}}{V_{cell}} P_x \cdot [x]_{out} \cdot e^{-\frac{F}{2RT} \cdot z_x \cdot V_m} \cdot \left(1 - e^{\frac{\Delta G_x}{RT}}\right) \tag{13}$$

which is equivalent to the equations (7) and (9) in the main text. If $b = 1$, $\frac{dV(z)}{dz} = \text{constant}$ across the membrane. This was assumed by Goldman to derive the Goldman–Hodgkin–Katz (GHK) flux equation, and it it reduces the SI Eq. (12) to:

$$j_{L,x} = -\frac{S_{cell}}{V_{cell}} P_x \frac{z_x F}{RT} \cdot V_m \frac{[x]_{out}}{1 - e^{\frac{z_x F}{RT} V_m}} \cdot \left(1 - e^{\frac{\Delta G_x}{RT}}\right) \tag{14}$$

If $V_m < 0$, $\Delta G_x < 0$, $j_{L,x} > 0$ species $x$ moves from the outside to the intracellular environment, as expected. As mentioned before, we use Eyring's assumption for our simulations and, for simplicity, we also assume that the surface partition coefficient $\frac{[x]_{out}^{(interface)}}{[x]_{out}^{(bulk)}}$ is constant, thus $P_x$ is a constant as well.

**Detailed derivation of SI equations (13) and (14)** To obtain Eqs. (13) and (14) from Eq. (12) we first notice that $\Delta G_x/RT = -u + \ln([x]_{in}/[x]_{out})$ so that Eq. (12) becomes:

$$\begin{aligned} j_{L,x} &= \frac{S_{cell}}{V_{cell}} P_x \cdot b \cdot u \frac{[x]_{out} e^{u/2}}{e^{bu/2} - e^{-bu/2}} \left(1 - \frac{[x]_{in}}{[x]_{out}} e^{-u}\right) \\ &= \frac{S_{cell}}{V_{cell}} P_x \cdot b \cdot u \frac{[x]_{out} e^{u/2}}{e^{bu/2} - e^{-bu/2}} \left(1 - e^{\frac{\Delta G_x}{RT}}\right) \\ &= \frac{S_{cell}}{V_{cell}} P_x \cdot b \cdot u \frac{[x]_{out}}{e^{(b-1)u/2} - e^{-(b+1)u/2}} \left(1 - e^{\frac{\Delta G_x}{RT}}\right) \end{aligned} \tag{15}$$

When $b = 1$, Eq. (15) is equivalent to:

$$j_{L,x} = \frac{S_{cell}}{V_{cell}} P_x \cdot u \frac{[x]_{out}}{1 - e^{-u}} \left(1 - e^{\frac{\Delta G_x}{RT}}\right) \tag{16}$$

Which is equivalent to Eq. (8) in [13].

In order to show how to obtain Eq. (13) from Eq. (12) we first introduce the hyperbolic sinus: $2 \cdot \sinh(bu/2) = e^{bu/2} - e^{-bu/2}$ such that Eq. (15) is written:

$$j_{L,x} = \frac{S_{cell}}{V_{cell}} P_x \cdot b \cdot u \frac{[x]_{out} e^{u/2}}{2\sinh(bu/2)} \left(1 - e^{\frac{\Delta G_x}{RT}}\right) \tag{17}$$

We then use the fact that $\lim_{b \to 0} \left(\frac{2\sinh(bu/2)}{b}\right) = u$ and consequently when $b \to 0$ Eq. (17) reduces to Erying's rate equation (13).

## Numerical simulations

The first step of our numerical experiment consists in finding parameter sets consistent with establishing a particular value of $V_{m,0}$, that is the membrane voltage in the absence of the dye. We assume that before the addition of the dye, the cell is in steady-state $\forall x : dx/dt = 0$ and consequently:

$$\frac{d[A^-]_{in}}{dt} = 0 \Leftrightarrow \Delta G_{L,A^-} = 0 \tag{18}$$

$$\frac{d[C^+]_{in}}{dt} = 0 \Leftrightarrow j_P = j_{L,C^+} \tag{19}$$

Thus, at steady-state, $A^-$ equilibrates according to Nernst Eq. (2) in the main text and $C^+$ according to Eq. (11) in the main text. Consequently, to obtain the $V_{m,0}$ we solve the following ordinary differential equation system in a 3-dimensional grid $\{\Delta G_E, [Y]_{in}, \rho\}$ (see SI Table 4):

$$\frac{d[A^-]_{in}}{dt} = 1 - e^{\frac{\Delta G_{A^-}}{RT}} \tag{20}$$

$$\frac{d[C^+]_{in}}{dt} = 1 - e^{\frac{\Delta G_{C^+}}{RT}} - \rho \cdot \left(1 - e^{\frac{\Delta G_P}{RT}}\right) \tag{21}$$

As shown in Fig. SI1, the influence of the dye on $\Delta V_m$ depends on how $V_{m,0}$ was generated, and we can achieve the same value of $V_{m,0}$ by different parametrizations of $\{\rho, \Delta G_E, [Y]_{in}\}$.

The second part of the numerical experiment consists of choosing a starting steady-state set of values for $\{V_{m,0}, \Delta G_E, [Y]_{in}\}$ and a given $[Dye]_{out}$. We also select the values for the permeability of the membrane to cations, anions and the dye ($P_{C^+}$, $P_{A^-}$ and $P_{Dye}$, respectively) and keep them fixed through out the experiment (values are given in SI Table 3). Lastly, to obtain the dye equilibration profile we need to implement the rate-laws for pumping and leakage we discussed above, and then solve the ODE system of SI equations (9) to (11) using the stiff solver "ode15s" from MATLAB R2018b. The initial *intracellular* concentration of the dye we chose is $[Dye]_{in} = 10^{-10} mM$, and the $k_P$ value is chosen based on the steady-state solution for $V_{m,0}$ and using Eq. (10) in the main text. Specifically, for a chosen set of $\{V_{m,0}, \Delta G_E, [Y]_{in}\}$ we find $\rho$ that gives $V'_{m,0} \approx V_{m,0}$ and use it to set $k_P$ from the definition of $\rho$ in Eq. (10) in the main text:

$$k_P = \frac{S_{cell}}{V_{cell}} \cdot P_{C^+} \cdot [C^+]_{out} \cdot \rho(V'_{m,0}) \cdot e^{-\frac{FV'_{m,0}}{2RT}}. \tag{22}$$

## Distinguishing the inner from the outer membrane

In the main text we assumed cell's cytoplasm is separated from the environment by one membrane, effectively ignoring any potential charge separation across the outer membrane of *E. coli*. While active transport of cations proceeds across the inner membrane for the case of *E. coli*, e.g. NhaA [18] or KefB/C [19], surface charge on the outer membrane can lead to Donnan potential [20, 21], and we call this trans-outer-membrane voltage $V_p$. In the absence of pumps moving cations between the periplasmic and extracellular space, the ions equilibrate across the outer membrane according to Nernst equation. Therefore, for the periplasmic concentrations we can write:

$$[C^+]_p = [C^+]_{out} \cdot e^{-\frac{F}{RT}V_p} \tag{23}$$

$$[Dye^+]_p = [Dye^+]_{out} \cdot e^{-\frac{F}{RT}V_p} \tag{24}$$

$$[A^-]_p = [A^-]_{out} \cdot e^{+\frac{F}{RT}V_p} \tag{25}$$

We used the measured value for $V_p \sim -30$ mV (negative in the periplasm) [21] to estimate $[Dye^+]_p \approx 3.2 \times [Dye^+]_{out}$. Thus, in the presence of such a $V_p$, the overall membrane voltage $V_m^\star$ would become $V_m^\star = V_m + V_p$ [11] and the impact of the dye on $V_m$ is as if there was no $V_p$ but the $[Dye_{out}]$ was $\sim 3.2$ times greater. Similarly, to account for the effect of the trans-outer-membrane voltage, all the concentrations $[x]_{out}$ refered to in the main text should be corrected by a factor $e^{-z_x \frac{F}{RT}V_p}$.

## REFERENCES


[1] N. Lord, *Fluctuation timescales in bacterial gene expression*. PhD thesis, Harvard University, 2014.

[2] T. Pilizota and J. W. Shaevitz, "Fast, multiphase volume adaptation to hyperosmotic shock by escherichia coli," *PLOS ONE*, vol. 7, pp. 1–10, 04 2012.

[3] E. Krasnopeeva, C.-J. Lo, and T. Pilizota, "Single-cell bacterial electrophysiology reveals mechanisms of stress-induced damage," *Biophysical Journal*, vol. 116, no. 12, pp. 2390 – 2399, 2019.

[4] Y. Wang, E. Krasnopeeva, S. Lin, F. Bai, T. Pilizota, and C. Lo, "Comparison of escherichia coli surface attachment methods for single-cell, in vivo microscopy," *In preparation*, 2019.

[5] M. Basan, M. Zhu, X. Dai, M. Warren, D. Sévin, Y.-P. Wang, and T. Hwa, "Inflating bacterial cells by increased protein synthesis," *Molecular Systems Biology*, vol. 11, no. 10, 2015.

[6] W. Bai, K. Zhao, and K. Asami, "Dielectric properties of e. coli cell as simulated by the three-shell spheroidal model," *Biophysical Chemistry*, vol. 122, no. 2, pp. 136 – 142, 2006.

[7] P. F. Costa, M. G. Emilio, P. L. Fernandes, H. G. Ferreira, and K. G. Ferreira, "Determination of ionic permeability coefficients of the plasma membrane of xenopus laevis oocytes under voltage clamp.," *The Journal of Physiology*, vol. 413, no. 1, pp. 199–211, 1989.

[8] J. Rosko, V. A. Martinez, W. C. K. Poon, and T. Pilizota, "Osmotaxis in escherichia coli through changes in motor speed," *Proceedings of the National Academy of Sciences*, 2017.

[9] K. A. Martinez, R. D. Kitko, J. P. Mershon, H. E. Adcox, K. A. Malek, M. B. Berkmen, and J. L. Slonczewski, "Cytoplasmic ph response to acid stress in individual cells of escherichia coli and bacillus subtilis observed by fluorescence ratio imaging microscopy," *Applied and Environmental Microbiology*, vol. 78, no. 10, pp. 3706–3714, 2012.

[10] E. Krasnopeeva, *Single cell measurements of bacterial physiology traits during exposure to an external stress*. PhD thesis, University of Edinburgh, 2018.

[11] M. Grabe and G. Oster, "Regulation of organelle acidity," *The Journal of General Physiology*, vol. 117, no. 4, pp. 329–344, 2001.

[12] R. Buda, Y. Liu, J. Yang, S. Hegde, K. Stevenson, F. Bai, and T. Pilizota, "Dynamics of escherichia coli's passive response to a sudden decrease in external osmolarity," *Proceedings of the National Academy of Sciences*, vol. 113, no. 40, pp. E5838–E5846, 2016.

[13] K. D. Garlid, A. D. Beavis, and S. K. Ratkje, "On the nature of ion leaks in energy-transducing membranes," *Biochimica et Biophysica Acta (BBA) - Bioenergetics*, vol. 976, no. 2, pp. 109 – 120, 1989.

[14] J. Keener and J. Sneyd, *Mathematical Physiology*, p. 93. 2009.

[15] J. E. Hall, C. A. Mead, and G. Szabo, "A barrier model for current flow in lipid bilayer membranes," *The Journal of Membrane Biology*, vol. 11, pp. 75–97, Dec 1973.

[16] W. Morf, *The Principles of Ion-selective Electrodes and of Membrane Transport*. Studies in analytical chemistry, New York, 1981.

[17] H. Butt, M. Karlheinz Graf, H. Butt, K. Graf, and M. Kappl, *Physics and Chemistry of Interfaces*. Physics textbook, Wiley, 2003.

[18] I. T. Arkin, H. Xu, M. Ø. Jensen, E. Arbely, E. R. Bennett, K. J. Bowers, E. Chow, R. O. Dror, M. P. Eastwood, R. Flitman-Tene, B. A. Gregersen, J. L. Klepeis, I. Kolossváry, Y. Shan, and D. E. Shaw, "Mechanism of na+/h+ antiporting," *Science*, vol. 317, no. 5839, pp. 799–803, 2007.

[19] M. Papanastasiou, G. Orfanoudaki, M. Koukaki, N. Kountourakis, M. F. Sardis, M. Aivaliotis, S. Karamanou, and A. Economou, "The escherichia coli peripheral inner membrane proteome," *Molecular & Cellular Proteomics*, vol. 12, no. 3, pp. 599–610, 2013.

[20] P. Nelson, *Biological Physics (Updated Edition)*. 2003.

[21] J. B. Stock, B. Rauch, and S. Roseman, "Periplasmic space in salmonella typhimurium and escherichia coli.," *Journal of Biological Chemistry*, vol. 252, no. 21, pp. 7850–61, 1977.